Peak Broadening Anisotropy and the Contrast Factor in Metal Alloys

Thomas Hadfield Simm

Materials Research Centre, Swansea University, Wales SA1 8EN, UK; thomas.simm@dmata.co.uk

Abstract: Diffraction peak profile analysis (DPPA) is a valuable method to understand the microstructure and defects present in a crystalline material. Peak broadening anisotropy, where broadening of a diffraction peak doesn't change smoothly with 2θ or *d*-spacing, is an important aspect of these methods. There are numerous approaches to take to deal with this anisotropy in metal alloys, which can be used to gain information about the dislocation types present in a sample and the amount of planar faults. However, there are problems in determining which method to use and the potential errors that can result. This is particularly the case for hexagonal close packed (HCP) alloys. There is though a distinct advantage of broadening anisotropy in that it provides a unique and potentially valuable way to develop crystal plasticity and work-hardening models. In this work we use several practical examples of the use of DPPA to highlight the issues of broadening anisotropy.

1. Introduction

The ability to quantify the shape of diffraction peak profiles is an important aspect of crystallography and materials science [1–3]. The technique can be used to quantify the dislocation density, crystal/dislocation-cell size, planar fault percentage and the dislocation slip systems present in samples in a statistically significant manner that is either practically very difficult or not possible using other techniques. However, its more widespread use is limited due to practical and mathematical limitations of the technique [4,5]. One of the main limitations of the technique is due to peak broadening anisotropy, which has implications on the results of the broadening methods and its use with other techniques. But conversely, this limitation may also provide a way to extend polycrystal plasticity models to incorporate details at the nano scale such as the activity and arrangement of dislocations, and hence provide a way to combine dislocation and work-hardening models with polycrystal plasticity models.

Although the original formulism from Rietveld [6] assumed that the broadening of a diffraction peak varied smoothly with its *d*-spacing, it has long been found that peaks close together in *d*-spacing can vary significantly in their broadening [7,8]. Various models have been constructed to account for this peak broadening anisotropy in Rietveld refinements due to the presence of crystallite and microstrain effects [7,9,10]. One of the earlier works on the use of diffraction peak profiles to study deformed metal alloys was by Stokes and Wilson [8]. Based on a model that broadening was due to distortion within a crystal, they derived a formula for strain broadening that could explain this observed broadening anisotropy. If it is assumed that the stress distribution is statistically isotropic, they showed that elastically anisotropic crystals (as even cubic crystal are) would lead to a strain that varied with crystallographic direction. The term is the same as that used today [11], although now this strain anisotropy is derived in terms of the presence of dislocations.

In metal alloys the most important cause of broadening is believed to be dislocations [12], with planar faults, such as stacking faults or twin faults, being the second most important contributor. Various models exist for how peak broadening anisotropy in a metal alloy can be accounted for, based mainly on the changes in dislocations and planar faults, these include: (a) the average character of dislocations in a sample, that is whether they are mainly edge or screw; (b) the average Burgers vector of dislocations in the sample; (c) the slip systems of the dislocation in different orientations found using a crystal plasticity model; (d) the dislocation density in different orientations; (e) the average amount of different planar fault types in a sample. In most cases broadening anisotropy is not directly addressed, but instead a method is applied only to improve the data analysis and reduce errors. Due to the number of different models to account for anisotropy it can be difficult to evaluate the best approach, and what the implications are of their use. This often means that the cause of the broadening anisotropy is just another fitting parameter which is used only to improve the data analysis and reduce errors.

Diffraction peak profile analysis (DPPA) is potentially a very powerful tool to probe the nano-structure of a metal alloy. However, a lack of understanding of the implications of how to address the broadening anisotropy can lead to errors and incorrect interpretation when applying DPPA methods. To address this issue, this paper seeks to answer the following questions: (1) is there a physical basis for this anisotropy in deformed metal alloys, or is it just a method to improve data analysis by using more diffraction peaks? (2) what are the implications of this anisotropy for diffraction peak profile analysis methods?

Supplementary data and analysis of this work can be found at Open Science Framework [13]. New analysis of data using DPPA methods in this review was done using the MATLAB graphical user interfaces BIGdippa and dippaFC (dippa_v3) [14].

2. Theory

2.1. The Contrast Factor

The displacement field around a dislocation is anisotropic (Figure 1). This is readily observed in transmission electron microscopy (TEM) imaging of dislocations, whereby rotating the sample so that a dislocation's Burgers vector (***b***) is perpendicular to the diffraction vector, ***g***, gives a vanishing contrast. The modelling of a dislocation's displacement field is an important method used within TEM to be able to identify details of dislocations [15,16], especially in cases when **g.b** = 0 does not lead to vanishing contrast or due to practicalities of rotating a sample. In the same manner, the diffraction broadening caused by a dislocation varies depending on the diffraction vector, and can be calculated by modelling the dislocation's displacement field. The contribution of a dislocation's displacement field to the broadening of different diffraction profiles is through what is known as the contrast (or orientation) factor of dislocations. The contrast factor of an individual dislocation is dependent on the angles between the diffraction vector and the vectors that define the dislocation: it's Burgers vector (***b***), slip plane normal (***n***), and dislocation line (***s***). The contrast factor of an individual dislocation can be calculated using the computer program ANIZC [17]. For example, the edge dislocation in Figure 2 has a contrast factor of 0.46 when ***g*** is [110] and parallel to the dislocations Burgers vector. The value is 0.00 when ***g*** is parallel to the slip line ($[1\bar{1}2]$) and 0.05 when ***g*** is parallel to the slip plane normal ($[\bar{1}11]$).

The way in which the contrast factor is incorporated into diffraction peak profile analysis (DPPA) techniques can be illustrated with the Williamson-Hall method [19]. Incorporation within other methods, such as the Warren-Averbach method [1] uses the same approach. The Williamson-Hall method [19] is a common method to define the broadening of a diffraction peak; here the full-width at half maximum intensity (full-width, or FW) of a diffraction peak is defined as being due to micro-strain and size components. In terms of broadening by dislocations this equation can be written as [4,20]:

$$FW_{hkl} = \frac{K_{Sch}}{D} + f_m g \sqrt{\left(\rho \overline{C_{hkl}}\right)} \tag{1}$$

where, D is the crystal size, K_{Sch} is the Scherrer constant (often taken as 0.9 for spherical crystals), g is the reciprocal of the d-spacing of a peak, f_m is a function related to the arrangement of dislocations (and represents how the arrangement of groups of dislocations influence their total strain), ρ is the dislocation density and $\overline{C_{hkl}}$ is the average contrast factor of dislocations in grains that contribute to the hkl diffraction peak. In Equation 1 and other DPPA approaches, $\overline{C_{hkl}}$ is assumed to be the only term that accounts for broadening anisotropy and its value is required to be able to obtain the dislocation density.
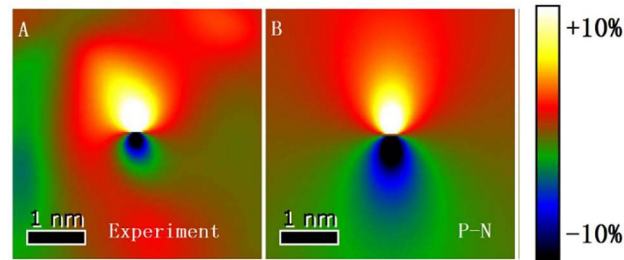
Figure 1. Experimental (**A**) and theoretical (**B**) strain fields around the edge component from a 60° dislocation core on a Ge/Si interface. Adapted from Liu et al. [15].
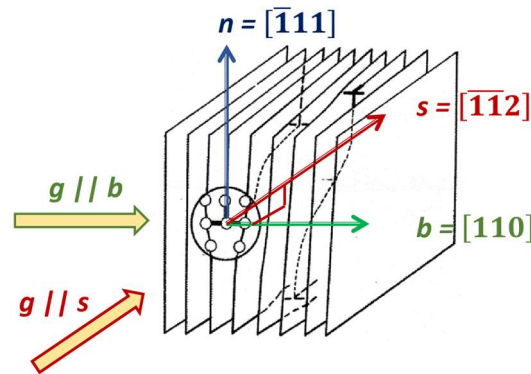
Figure 2. Schematic of an edge dislocation in a face-centred cubic crystal. The dislocation will cause maximum broadening when the diffraction vector is paralell to [110] and a minimum when it is parallel to $\left[1\overline{1}2\right]$. For the dislocation shown b is [110], n is $\left[\overline{1}11\right]$, and s is $\left[1\overline{1}2\right]$. Adapted from Armstrong [18].

As discussed by Scardi, Leoni and Delhez [21], the use of Williamson-Hall methods can be problematic for quantitative peak profile analysis, such as in determining details about broadening anisotropy and contrast factors, which is particularly relevant here. In addition, the use of the full-width is limited because it does not account for the whole of a peak profile. This can be especially important when broadening is due to dislocations, as shown by Wilkens [22] the same full-width can be caused by very different dislocation arrangements. A better parameter than the full-width, because it accounts for all the peak is the integral breadth, which is the area under a diffraction peak divided by the peaks height. The integral breadth can be replaced by the full-width in Equation (1) and in other Williamson-Hall equations. Due to their common use, both the full-width and the Williamson-Hall method are used throughout to display broadening anisotropy. The implications of this approximation are discussed by comparing full-width data, with integral breadths and Fourier coefficients of a titanium alloy in a later section (Section 3.2.1).

2.2. Contrast Factor, Homogeneous Approach

2.2.1. Cubic Alloys

For a powder diffraction pattern, a particular diffraction peak consists of contributions from many different crystals, of different orientations and containing a variety of different dislocation types.

Hence, to calculate the contrast factor for different diffraction peaks assumptions about the dislocations present are required. If it is assumed that, the sample has a random texture (no preferred orientation) and that slip system types, with a given Burgers vector and slip plane such as [110] (111) in face-centred cubic (FCC) crystals, are equally populated. This leads to a description for the contrast factor for a cubic material given as [11]:

$$\overline{C} = C_{h00}\left(1 - qH^2\right),\tag{2}$$

where

$$H^2 = \frac{h^2k^2 + h^2l^2 + k^2l^2}{\left(h^2 + k^2 + l^2\right)^2}$$

C_{h00} and q are constants that are dependent on the elastic constants of the material and the dislocations present and h, k, l are the indices of the diffraction peak.

The value of q is used as a fitting parameter in DPPA methods, such as the modified-WH and modified-WA methods [19,20,23]. The value obtained from the fitting can be used to quantify the amount of different dislocation types since they also have different q values. For example, in stainless steel the q values for edge and screw dislocations are 1.72 and 2.47 [3,17], hence a fitted q value of 2.10 would be interpreted as the sample consisting of 50% screw and 50% edge dislocations. The homogeneous contrast factor approach has been widely used to quantify cubic alloys. Including, the amount of edge or screw dislocations [24–28], or the relative quantities of different slip types [29] in cubic crystals.

2.2.2. Hexagonal Close Packed Alloys

In a similar manner to that seen in Equation (2) for cubic crystals, Dragomir and Ungar [30] provided a formula for the contrast factor for hexagonal close packed (HCP) metals:

$$\overline{C} = \overline{C_{hk.0}}\left(1 + q_1 x + q_2 x^2\right),\tag{3}$$

where

$$x = \frac{2l^2}{3(ga)^2}$$

$\overline{C_{hk.0}}$, q_1 and q_2 are constants that are dependent on the elastic constants of the material and the dislocations present, $g = 1/d$, l is the 3rd hkl index, and 'a' one of the lattice parameters (the HCP notation {$hkil$} is used but ignoring the 'i' index). As with the cubic formula the values of q are used as fitting parameters, which have a physical meaning. The method, described in more detail in [30], assumes that for a particular slip system type (such as <a> slip on the basal plane, or basal <a>), dislocations are equally populated (i.e., (0001) $[1\overline{2}10]$ has the same activity as (0001) $[\overline{2}110]$ and the other basal <a> slip systems). However, different slip system types are allowed to have different activities. Each slip system type has its own set of q values and values of $\overline{C_{hk.0}}$. The method then works by comparing the measured q values to those of the different slip system types, the amount of <a>, <c+a> and <c>, to determine their activity. The slip systems are grouped (Figure 3 and Table 1) into edge dislocations of the main slip systems in HCPs, and screw dislocations of the three Burgers vector types: <a>, <c+a> and <c>. From the q values of the different slip systems there is a greater tendency for <c+a> dislocations to have $q_1>0$ and for <a> dislocations to have $q_1<0$; in addition, prismatic <a> and pyramidal <a> are the only dislocations with $q_1<0$ and $q_2>0$. Hence, if the measured q_1 is less than 0 the method will provide <a> dislocations as the dominant dislocation type, and if the measure q_2 is more than 0 the value of <a> dislocations will be predicted to be close to 100%. Modifications to the approach have been made by some researchers to only include expected dislocation types; such as done by Seymour et al. for neutron irradiated zirconium alloys [31] using calculated contrast factor values for common dislocations found in the alloy, but the approach thereafter is essentially the same.
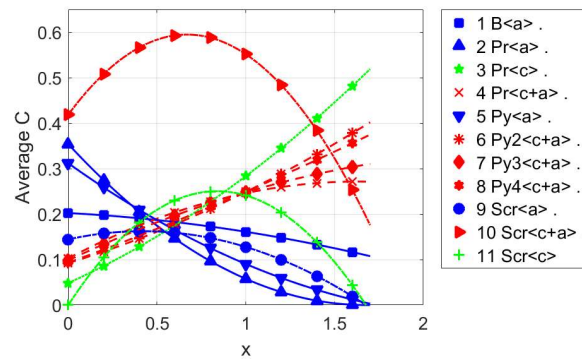
Figure 3. The change in the average contrast factor for the most common slip systems of titanium at different *x* values. The *q* values of the slip systems are detailed in Table 1. Adapted from Dragomir and Ungar [30].

Table 1. The *q* values and $\overline{C_{hk.0}}$ values for the most common slip system types of titanium. Data from Dragomir and Ungar [30].

Slip System Type	Slip Plane	Burgers Vector	$\overline{C_{hk.0}}$	q_1	q_2
1. Basal <a>	(0002)	$[11\bar{2}0]$	0.20227	−0.101142	−0.102625
2. Prismatic <a>	$(1\bar{1}00)$	$[11\bar{2}0]$	0.35387	−1.19272	0.355623
3. Prismatic <c>	$(1\bar{1}00)$	[0001]	0.04853	3.6161928	1.2264112
4. Prismatic <c+a>	$(1\bar{1}00)$	$[11\bar{2}3]$	0.10247	2.017177	−0.616631
5. Pyramidal <a>	$(10\bar{1}1)$	$[11\bar{2}0]$	0.3118	−0.894009	0.1833109
6. Pyramidal2 <c+a>	$(11\bar{2}2)$	$[11\bar{2}3]$	0.09227	1.299046	0.3972469
7. Pyramidal3 <c+a>	$(11\bar{2}1)$	$[11\bar{2}3]$	0.09813	1.89412	−0.365739
8. Pyramidal4 <c+a>	$(10\bar{1}1)$	$[11\bar{2}3]$	0.09323	1.5270212	0.14615
9. Screw <a>	multiple	$[11\bar{2}0]$	0.1444	0.59492	−0.710368
10. Screw <c+a>	multiple	$[11\bar{2}3]$	0.41873	1.25714	−0.94015
11. Screw <c>	multiple	[0001]	3.61×10^{-6}	165366	−98611

Whereas, in cubic alloys the value of the constant C_{h00} is very similar for edge and screw dislocations, in HCP alloys the corresponding constant $\overline{C_{hk.0}}$ can vary significantly for different slip systems. Therefore, in HCP alloys the contrast factor cannot just be a fitting variable, because it is needed to evaluate the dislocation density. This can be seen from Equation (1), which shows a feature of DPPA methods that they can only obtain the product $\rho\overline{C_{hkl}}$ and not the values individually. The homogeneous contrast factor approach has been widely used in HCP alloys to quantify the fraction of dislocations with different Burgers vectors [3,22,29–33]., or relative amounts of slip systems with different slip planes [3,30].

2.3. Planar Faults

Planar faults are defects in the crystal structure that are caused when the regular stacking of atoms is interrupted. Planar faults can be separated into two main types: stacking faults and twin faults. The presence of planar faults on diffraction peaks has been investigated in several works [23,32–35], with the work of Warren [23] being the most widely used for metal alloys.

In the approach of Warren, the contribution to broadening is given by adding an additional element to the size broadening. Hence, $1/D$ in Equation (1) is replaced with $1/Deff$ [23]:

$$\frac{1}{Deff_{hkl}} = \frac{1}{D} + \frac{(1.5\alpha + \beta)}{a}\varpi_{hkl},\tag{4}$$

where *a* is the unit cell size, ϖ_{hkl} is a constant for a particular diffraction plane and given in Table 2, α the stacking (intrinsic stacking fault or deformation) fault probability and β the twin probability. The value of α and β are the fraction of crystal's layers that are of the planar fault types.

Warren [1] also showed that planar faults would also cause shifts in the position of a diffraction peak and a change in a peak's asymmetry. The magnitude of the shit in a peak was given by the following formula:

$$\Delta 2\theta = \frac{\sqrt{3}\alpha \tan\theta \chi_{hkl}}{2\pi}, \tag{5}$$

which can be converted to

$$\Delta g_{hkl} = \frac{\sqrt{3}}{4\pi}\alpha g_{hkl}\chi_{hkl}$$

where, χ_{hkl} is a constant for a given hkl plane and given in Table 2.

Balogh, Ribarik and Ungar [34] developed an analytical description of planar faults in FCC crystals to incorporate within the MWP diffraction peak profile analysis fitting program [36]. The procedure used the same formulism as Warren but was calculated with the computer program DIFFAX [32]. The approaches of Warren and Balogh et al. can both be used to estimate the broadening, peak profile asymmetry and shifts in the peaks. The main difference is that in the Balogh et al. approach the planar faults are separated into three types of faults: intrinsic and extrinsic stacking faults, and twin faults. Several authors have used the formulae of Warren [28,37] and that of Balogh et al. [38,39] to describe planar faults.

A formulism for twinning in HCP alloys was introduced by Balogh, Tichy and Ungar [40], in a similar manner to the work on planar faults in cubic alloys [34], using DIFFAX [32] and based on the boundaries of twins. The formulism has been used to quantify twinning in a magnesium alloy [41].

In the same manner as the contrast factor, there are multiple planes that planar faults can reside on; depending on the plane and the diffraction vector the contribution to broadening will be different. Hence, like the approach used with the contrast factor, it is often assumed that all planes are equally populated. Both planar fault broadening and dislocation broadening will give rise to anisotropic broadening, however there are differences between the two. Firstly, planar fault broadening is a type of 'size' broadening because it is doesn't have a dependence with *g* unlike 'strain' broadening. So, for example the 200 and 400 peaks are both broadened the same amount by planar faults, but not by the strain from dislocations. Secondly, planar faults can cause peak asymmetry and the shifting of the position of diffraction peaks, which does not occur in standard dislocation broadening formulae.

Table 2. The values of parameters ϖ_{hkl} used in Equation (4) and X_{hkl} used in Equation (5), for quantifying the planar fault fraction to broadening in FCC alloys [23].

hkl	111	200	220	311	222	400
ϖ_{hkl}	$\frac{\sqrt{3}}{4}$	1	$\frac{1}{\sqrt{2}}$	$\frac{3}{2\sqrt{11}}$	$\frac{\sqrt{3}}{4}$	1
X_{hkl}	$\frac{1}{4}$	$\frac{-1}{2}$	$\frac{1}{4}$	$\frac{-1}{11}$	$\frac{-1}{8}$	$\frac{1}{4}$

2.4. Contrast Factor, Plasticity Approach

In the plasticity approach to calculate the contrast factor, it is assumed that different grains have different dislocation populations that are calculated using a polycrystal plasticity model [42–44]. Polycrystal plasticity models are mathematical models of how polycrystals respond to an applied load. They can be used to predict various changes in a material due to plastic deformation: (1) changes in orientations [45,46], (2) the spreading of orientations [47], (3) intergranular strains [48], (4) dislocation and twin types present [42]. The simplest and most widely used models are the Taylor model [49] and the Schmid factor / Sachs model [50], but the use of more advanced models, such as visco-plastic self-consistent (VPSC) and crystal plasticity finite element models (CPFEM) [51,52], has increased significantly due to increased computational power and the accompanying development

and availability of these models to researchers. These models do not provide dislocation density values, but instead provide the amount of slip on different slip systems. Therefore, to convert slip to dislocation density we need to make two main assumptions. Firstly, an assumption is needed about the relationship between slip activity and dislocation density of a particular slip system. One way to do this is by using the Orowan equation [53], as used in a few works to calculate the contrast factor [42–44], which relates an increment of shear (γ_i) on a slip system *i* to the increase in the mobile dislocation density on that system (ρ_m^i), based on the magnitude of the dislocation's Burger vector (b^i) and the dislocations speed (V^i).

$$\dot{\gamma}^i = \rho_m^i b^i V^i, \tag{6}$$

Two further assumptions are then taken. Firstly, about the screw or edge nature of the dislocations, which for simplicity it is often assumed that they have the same probability. Secondly, an assumption is needed about dislocation reactions, such as annihilation and cross-slip; the simplest ways to do this is by either assuming there are no dislocation reactions or that dislocations get distributed randomly to all slip systems with increments of strain. The actual situation is far more complicated than given by this equation and the two assumptions presented. Plastic deformation represents a complex and chaotic system, and as expressed succinctly by Alan Cottrell in 2002 [54] is the most challenging problem faced within classical physics. It is hoped that the development of dislocation models (such as dislocation dynamic models [55,56]) will aid with providing better formulation between slip activity from polycrystal models and details of dislocations such as their density, arrangement and the planes and Burgers vectors they have.

Each slip system in each grain will have a corresponding contrast factor that will differ depending on the diffraction plane being measured. Hence, to determine the average contrast factor for a diffraction peak involves finding the contrast factor of each dislocations that contributes to a peak and taking the average of these values. The individual contrast factors can be found using a program such as ANIZC [17] and the averaging can be done based on the texture. From this averaging, contrast factor values are obtained that depend on both the diffraction plane and the angle of that diffraction plane relative to the imposed load.

3. Practical Examples

3.1. Cubic Alloys

3.1.1. Homogeneous Approach

In the work of Simm et al. [4] two face-centred cubic (FCC) alloys, stainless steel and a commercially pure nickel, were deformed by compression to a range of applied strains. The samples were then measured using a laboratory X-ray diffractometer and subsequently analysed using different DPPA methods (more details are provided in [4]). The changes in the *q* values from three different modified Williamson-Hall analyses is shown in Figure 4. The data is relatively noisy and different *q* values are found depending on the Williamson-Hall equation used. Given these drawback, two main trends are observed.

Firstly, both alloys have falling *q* values with applied strain. This may be expected in stainless steel because at low strains there can be more screw dislocations due to the greater mobility of edge dislocations, whilst at higher strains dislocation interactions and activation of secondary slip systems can increase the relative amount of edge dislocations [57]. Partial dislocations are a feature of the dislocations in many alloys particularly those with a low stacking fault energy (SFE) in FCC alloys, such as stainless steel. Since partial dislocations have a lower *q* value than the full dislocation, the fall may also be due to a transition to partial dislocations. In nickel alloys recovery during plastic deformation results in the annihilation of screw dislocations and the formation of low-angle boundaries consisting of edge dislocations [57–59].
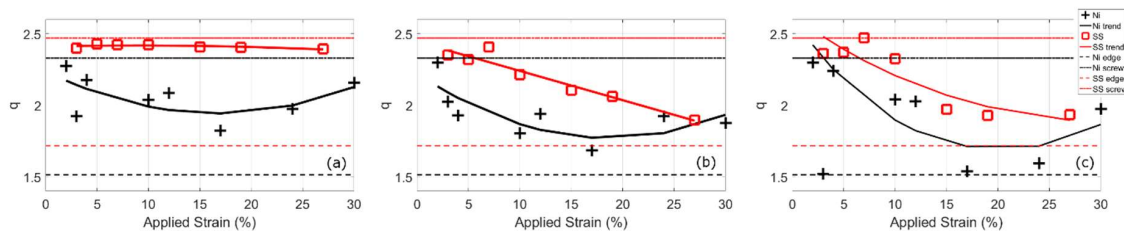
Figure 4. The change in *q* with applied strain of compression tested nickel and stainless-steel alloys. The lines indicate the predicted values for 100% edge and 100% screw dislocations for the two alloys using Equation (2) and ANIZC [17]. The different figures represent results using different modified Williamson-Hall methods; in the terminology of Simm et al. (**a**) is mWH-1, (**b**) mWH-2, and (**c**) mWH-3.

Secondly, the measured *q* values for nickel are closer to their calculated edge *q* values than that seen with the steel. This could be due to the dislocation structures that develop in high SFE alloys, consisting predominantly of edge dislocations [57].

Therefore, although most researchers do not use the *q* values to quantify the microstructure, there is reasonable justification from Figure 4 that *q* can be used to qualitatively evaluate the dislocation types in a sample, as also found by other researchers [24,60,61].

There is an additional benefit to the use of the contrast factor in this way, along with the details it provides of the microstructure, such as the edge to screw ratio. This is that it means that more diffraction peaks can be used during analysis. In FCC alloys, using a standard laboratory X-ray diffractometer, five diffraction peaks can be measured with two that are different orders of the same reflection, 111 and 222. Following the traditional method of using peaks of the same reflection can be problematic because of the relatively low intensity of the 222 peak, as well as the use of less diffraction peaks. An example of the difference between using the traditional and modified (with the contrast factor) approaches is shown in Figure 5, which shows the change in dislocation density using the Warren-Averbach method [4]. The figure shows that using the modified approach reduces the scatter, as given by the deviation from the best fit line. In addition, because different peaks are used that represent different orientations, the results should be more characteristic of the sample as a whole. The slightly different values obtained in some cases shown in the figure may be a result of this greater sampling of the sample.
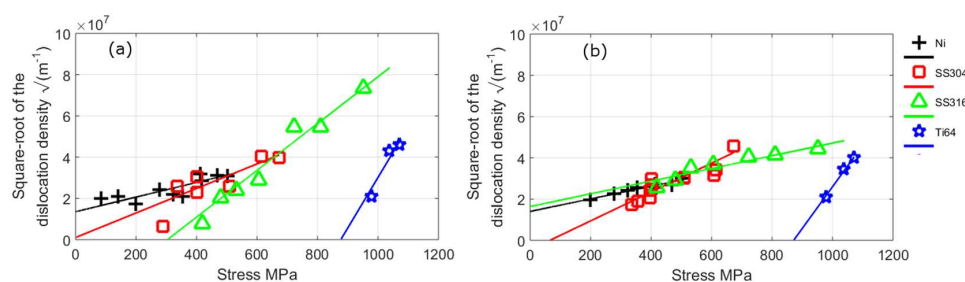

Figure 5. Plots of the change in dislocation density found by Warren-Averbach methods with applied deformation of compression and tensile samples, the stress the samples were at before unloading is shown. A commercially pure nickel alloy, two stainless steel alloys (304 and 316), and a titanium alloy (Ti-6Al-4V) are shown. In (**a**) the traditional approach is used, and in (**b**) the modified approach using the contrast factor is shown. Modified from Simm et al. [4].

3.1.2. Planar Faults

Dislocations are the most important defect contributing to the broadening of peaks in metal alloys, because of their importance in plastic deformation and how they contribute to broadening. The second most important defects are planar faults, as they are believed to be the only other defects in metals that

cause significant peak broadening [12]. Other defects such as point defects or second phase particles have strain fields that fall off with distance at a higher rate than the reciprocal of the distance squared, and will not in general cause significant peak profile broadening. Planar faults can be separated into three different types: twin faults, and extrinsic and intrinsic stacking faults. Deformation twinning [62] is an important mode of deformation in HCP alloys [63–65] and cubic alloys with a low stacking fault energy (SFE) such as stainless steel alloys [66,67], whilst in martensitic alloys the lath boundaries can be a twin boundary rather than a dislocation one [68]. Stacking faults also play an important part in the plastic deformation of an alloy [69]. During plastic deformation dislocations can dissociate into two partial dislocations connected by an intrinsic stacking fault, as the partial dislocations can sometimes move more easily than the full dislocation [57]; dissociation occurs more readily in alloys with a low stacking fault energy (SFE). Hence, the ability to quantify planar faults is an important tool for studying plastic deformation. However, because of the small size of planar faults (of the order of the lattice spacing) they are difficult to characterise and quantify.

DPPA techniques are a valuable tool for quantify planar faults in a statically significant manner. As shown in Figure 6, planar faults influence a number of aspects of a diffraction peak including, (a) the peak's broadening, (b) the asymmetry of a peak, and (c) the shift of a peak's position. The figure also shows that the different types of planar faults change the peak in different ways. The values in the figure were calculated using the formulae of Warren [23] (Equation (4)) and derived from the work of Balogh et al. [34] using a fault probability of 5% (the calculations are shown in [13]). For the planar fault calculations using the work of Balogh et al., the planar broadening is convoluted with a theoretical instrumental broadened peak, the full-width of this instrumental peak is deducted from the convoluted peak to give only broadening from planar faults in the figure. The change in the peak profiles of the first six FCC diffraction peaks using the formulism of Balogh et al. are shown in Figure 7, for intrinsic stacking faults and twin faults.
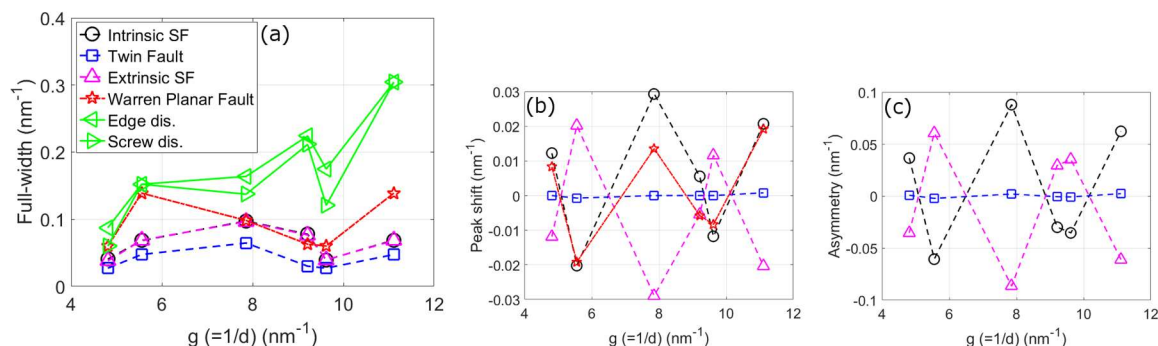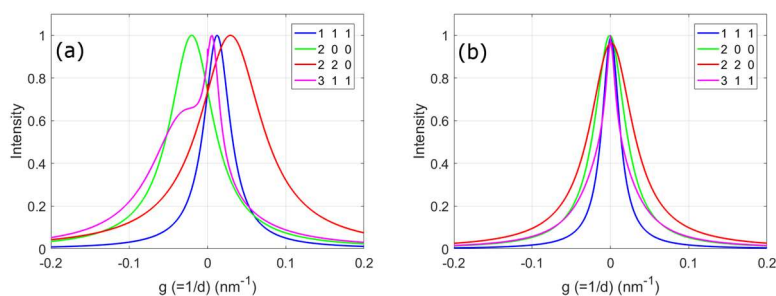

Figure 6. The effect of planar faults on the full-width (**a**), peak shift (**b**), and asymmetry (**c**) for the first six diffraction peaks of a FCC sample (111, 200, 220, 311, 222, 400). The intrinsic stacking faults and twin faults are determined using [34] convoluted to an instrumental broadened peak, and the instrumental FW is subtracted from the final FW. The Warren planar faults use formula from [23]. Values are for a fault probability of 5%. In (**a**) the broadening due to edge and screw dislocations using formula in [11] with a strain value to match the other values.

Reformulated values of ϖ_{hkl} used in Equation (4) and X_{hkl} used in Equation (5) using Balogh's approach are shown in Table 3. These values along with the accompanying equations provide an additional way to use the approach of Balogh et al., in addition to its part of the MWP procedure [36]. From this table and Figure 6, it can be seen that the approaches of Warren and Balogh et al. provide similar but markedly different results. Note that Warren's formula for broadening (Equation (4)) uses both intrinsic and twin faults, whereas the peak shift formula (Equation (5)) only uses intrinsic faults. The broadening from stacking fault and twin fault using the approach of Balogh et al. are similar, but stacking faults cause more broadening. The magnitude difference of twin and stacking faults

is consistent with Warren's formula in Equation (4) where stacking faults contribute 1.5 times the broadening of twin faults. Warren's formula gives a greater broadening of the 200 peak than with Balogh's approach, but the broadening of other peaks is closer. The peak shift changes are relatively close for the two approaches, particularly for 111 and 200 peaks. The biggest difference in the approaches is for asymmetry. Whereas, the work of Warren suggested that only twin faults should cause asymmetric peaks, this is the opposite of that found using Balogh's approach. Warren only defined asymmetry in terms of the 200 peak and commented that it is not possible to determine fault probability accurately from peak asymmetry, and is therefore not included in the figure.

Figure 7. The effect of planar faults on the peak profile of the first four diffraction peaks of a FCC sample (111, 200, 220, 311). The figures are for intrinsic stacking faults (**a**) and twin faults (**b**) using the formulism of Balogh et al. [34] and convoluted to a theoretical instrumental broadened peak.

Table 3. The values of parameters ϖ_{hkl} used in Equation (4) and X_{hkl} used in Equation (5), for quantifying the planar fault fraction to broadening in FCC alloys [23]. The values ae calculated based on the formulism given by Balogh et al. [34], those by Warren [1] are shown for comparison.

Constant	Planar Fault Type	111	200	220	311	222	400
ϖ_{hkl}	Intrinsic fault	0.291	0.491	0.701	0.558	0.283	0.496
	Twin	0.195	0.342	0.465	0.217	0.195	0.341
	Extrinsic fault	0.274	0.495	0.696	0.552	0.284	0.491
	Warren	0.433	1.000	0.707	0.452	0.433	1.000
X_{hkl}	Intrinsic fault	0.368	−0.527	0.542	0.087	−0.178	0.271
	Twin	0	−0.019	0	0	0	0.010
	Extrinsic fault	−0.354	0.530	−0.532	−0.085	0.177	−0.265
	Warren	0.250	−0.500	0.250	−0.091	−0.125	0.250

There are several practical problems in being able to use DPPA techniques to quantify planar faults in cubic crystals. The way in which twin and stacking faults contribute to broadening (as shown in Figure 6) means it is very difficult to calculate values for both without making additional assumptions (such as the relative amount of each). However, a bigger problem is separating broadening anisotropy due to planar faults and dislocations. This is particularly a problem when fitting multiple peaks as demonstrated in Figure 8. The figure shows a way to visualise broadening anisotropy caused by dislocations with different q-values (using Equation (2)) and the presence of planar faults (using Equation (4)). The modified Williamson-Hall plots in this figure are for nickel and stainless-steel samples deformed by compression to 10% applied strain. The data is taken from a neutron diffraction experiment at HRPD, ISIS, Oxfordshire detailed in [3,42], but unlike the figures in those works the full-width values shown are averaged over a range of angles between the tensile and diffraction vector. Different q-values causes the value of $gC^{0.5}$ of a peak to shift by different amounts relative to the position of the 200 (and 400) peak, which stays in the same position. Whilst, in the figure, the broadening from planar faults causes reductions in the broadening depending on the peak (and value of ϖ_{hkl}, see Table 3). Hence, the q values cause movement of data points in the x-direction ($gC^{0.5}$), whereas planar faults cause movement of the data points in the y-direction

(integral breadth). The success with which a definition describes the broadening anisotropy, can be given by the nearness to a fitted straight-line in Figure 8, root-mean-squared-errors of the data to the fitted lines are given in Table 4. The figure and accompanying table illustrates the difficulty that is encountered when trying to describe broadening anisotropy in terms of both *q* values and planar faults. For example, the root-mean-squared-errors can be very similar for very different descriptions of broadening anisotropy, such as those between edge and screw dislocations of nickel in the table. This problem is exacerbated because the description of broadening anisotropy by dislocations or planar faults are only an approximation, different descriptions of broadening anisotropy would be given by using different Williamson-Hall equations, or Warren-Averbach equations as shown in Figure 4. These difficulties are why it is common to only fit to either the q-value or only for planar faults.
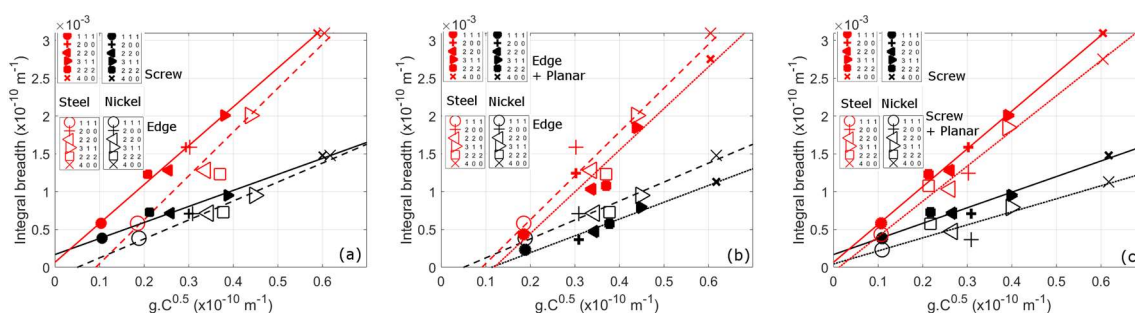
Figure 8. Modified Williamson-Hall plots of integral breadth against $gC^{0.5}$ for nickel and stainless-steel samples deformed to 10% applied strain. In (**a**) plots for different values of *q* of 1.5 (approximately edge) and 2.5 (approximately screw) using Equation (2). In (**b**,**c**) shows the effect of planar faults on the values in (**a**). The integral breadths are reduced by broadening from planar faults from Equation (4) of $\frac{(1.5\alpha+\beta)}{a}\wp_{hkl}$, using a nominal value of $1.5\alpha + \beta = 5.10^{-4}$. Straight lines have been fitted to the integral breadth against $gC^{0.5}$ for the different sets of values. The root-mean-squared-error (rmse) values for each of these are shown in Table 4. The data is for neutron diffraction measurements taken at HRPD, ISIS, Oxfordshire taken from [3]. The values are averaged over angles between the compression and diffraction vectors, between 0 and 90°.

Table 4. The root-mean-squared-error (rmse) values for the straight-line fits shown in Figure 8. For edge dislocation calculations *q* is taken as 1.5, for screw dislocations taken as 2.5, and for mixed as 2.0.

Alloy	Edge	Screw	Mixed	Edge + Planar Faults	Screw + Planar Faults	Mixed + Planar Faults
Steel	28.3×10^{-5}	6.8×10^{-5}	14.1×10^{-5}	22.1×10^{-5}	17.8×10^{-5}	10.3×10^{-5}
Nickel	7.1×10^{-5}	7.7×10^{-5}	2.9×10^{-5}	5.8×10^{-5}	13.6×10^{-5}	8.7×10^{-5}

Instead of using a whole powder diffraction profile approach (as shown in Figure 8), the planar faults can instead be determined from different orders of the same peak. These approaches are less prone to the problems presented above of incorporating planar faults as another fitting variable within a multiple peak fitting algorithm. In addition, they sample grains of the same orientation with the same strain distribution relative to the diffraction vector, which helps to reduce the problems with broadening anisotropy discussed in the next section, which are due to the heterogeneity of plastic deformation.

The crystal size broadening from different hkl reflections can be used to quantify the amount of planar faults using Equation (4). Since the crystal size (*D*) is not known, this means from Equation (4) that the size values from two different reflections are required (e.g., 111/222 and 200/400). The value

of the planar fault density can be found by rearranging Equation (4), and assuming crystal size broadening is a constant for all peaks, to give:

$$(1.5\alpha + \beta) = a\frac{(1/Deff_{200}) - (1/Deff_{111})}{(\varpi_{200} - \varpi_{111})},\tag{7}$$

In Figure 9 are Williamson-Hall plots of the same nickel and stainless-steel samples, compression tested to 10% applied strain, used above. The lines in the plot are Williamson-Hall fit lines (using g^2 against *FW*) for the 200/400 and 111/222 peaks of the alloys. The values of $(1/Deff_{200})$ and $(1/Deff_{111})$ are the intercepts of the lines in this figure.

In a similar manner Equation (5) needs to be rearranged to provide to provide an equation to quantify planar faults in deformed alloys. The intergranular strains, or the position of a diffraction peak, of a sample change due to plastic deformation, and can be predicted by crystal plasticity models [48]. The modelling is normally done on changes in intergranular strains during an in situ test (i.e., when there is an applied load), although these strains are less after unloading they are still present as shown in Figure 10. Since the intergranular strains due to plastic deformation are not generally known, it is not sufficient to use Equation (5) with a single diffraction peak and the lattice spacing measurement from an un-deformed sample. Instead the equation can be rearranged to give the intrinsic stacking fault fraction in terms of the difference in intergranular strains of two orders, as follows:

$$\alpha = \frac{4\pi}{\sqrt{3}(\chi_{111} - \chi_{222})}(\Delta g_{111}/g_{111} - \Delta g_{222}/g_{222}),\tag{8}$$

The quantity of planar faults in the nickel and stainless samples were found using Equation (7) (combined with Equation (1), i.e., using g not g^2 as shown in Figure 9) and Equation (8), and are shown in Table 5. The calculations were done using the average integral breadth, and average change in $\Delta g/g$ across the angles measured (between 0 and 90°). The values of planar faults in stainless steel are ~0.15%, whereas those for nickel are close to zero and often negative indicating the expected changes given by planar faults is not met. These results are consistent with the expectation that the quantity of planar faults is higher in stainless steel than in nickel. In addition, although not quantified the asymmetry changes shown in Figure 10 which show a greater difference in asymmetry between 111 and 222 peaks, or 200 and 400, in steel than in nickel is also consistent with these results. The change in intergranular strains of 200 and 400 peaks of stainless steel are unusual as they change in the opposite way than expected, i.e., g/g is higher for 200 the opposite of what is expected from the values in Table 3). This leads to a negative value for the fault percentage, although the absolute magnitude of the value is close to that found from the 111/222 peaks.

Table 5. The values of stacking fault (α) and twin faults (β) of stainless steel deformed to 10% applied strain using the data in Figures 9 and 10. The values ae calculated based on Equations (7) and (8) using values in Table 3 found from work of Balogh et al. [34], and Warren [1]. The values are given as percentages.

Alloy	Peaks	Warren Broadening (1.5α+β)	Balogh Broadening (1.5α+β)	Warren Intergranular strains (α)	Balogh Intergranular strains (α)
Steel	111/222	0.091	0.298	0.187	0.129
	200/400			−0.145	−0.137
Nickel	111/222	−0.058	−0.191	−0.059	−0.040
	200/400			−0.008	−0.007

There is an additional advantage of using the approach shown here to calculate planar faults. This is that the use of both the peak position and peak broadening can in theory offer a way to separate stacking and twin faults. Further investigation on alloys with known changes in these two could be

used to establish whether this is possible, whether peak asymmetry is due to twin or stacking faults, and which constants are best to use in Equations (7) and (8).
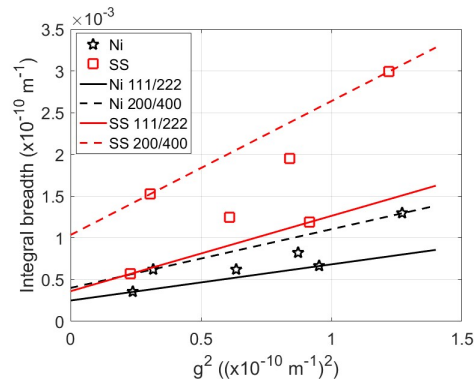
Figure 9. The full-width of the first six diffraction peaks (111, 200, 220, 311, 222, 400) of nickel and stainless-steel samples deformed to 10%. The data is for neutron diffraction measurements taken at HRPD, ISIS, Oxfordshire taken from [3]. The values are averaged over angles between the compression and diffraction vectors, between 0 and 90°.
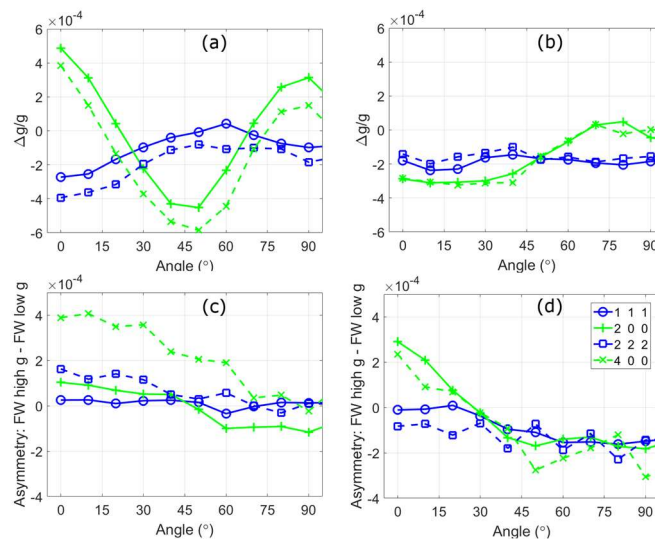
Figure 10. The measured peak positions and peak assymetry of a stainless steel (**a**,**c**) and nickel (**b**,**d**) alloy after compression testing to 10% applied strain, at different angles between the compression direction and the diffraction vector [3,42]. The change in peak position (**a**,**b**) are relative to the peak positions of an undeformed sample. The assymetry of a peak (**c**,**d**) is found from a pseudo-Voigt which has different full-width values either side of it's centre, the assymetry parameter is the full-width of the high *g* side minus the full-width of the low *g* side.

3.1.3. Plasticity Approach

In Figure 11 are full-width plots of compression deformed nickel and stainless-steel alloys at different applied strains. The figure is plotted at different angles between the compression direction and the diffraction vector, and shows that the full-width of a diffraction peak can vary significantly at the different angles. For example, for stainless steel after 10% strain the full-width of the 111 peak falls by ~20%, the 200 peak by ~20% and the 220 peak increases by ~40% from the values at 0°. Whereas for nickel after 10% strain, the full-width of the 111 peak falls by ~20%, the 200 peak by ~30% and the 220 peak increases by ~25% from the values at 0° These variations exist at all strains measured, and for

both the fatigue and compression samples shown in the figure. Furthermore, the same broad changes in the diffraction peak broadening with angle is observed for all samples. Since, the magnitude of the full-width values at 2% strain are lower the relative error in the full-widths will be higher, which may explain the slight difference to the higher applied strains. The broadening anisotropy with angle are observed for both the low stacking fault energy stainless-steel and the high stacking fault energy nickel; including a fall in the full-width of most peaks from 0° to 90°, minima for 200 and 111 peaks near 45°, and maxima for the 220 peak near 45°.

There are a number of possible causes for these changes in broadening with angle: (1) variations in dislocations density in different orientations; (2) variations in the arrangement of dislocations in different orientations which can contribute to broadening through both crystal size and dislocation arrangement [4]; (3) variations in the dislocation slip systems present (or slip anisotropy); (4) variations in the character of dislocations, i.e., whether they are edge or screw, in different orientations; (4) variations in other defects, such as planar faults, in different orientations; (5) variations in the spread in the intergranular strains in different orientations. The plasticity approach predictions of the contrast factor shown in Figure 12 is based on No. 3, variations in the dislocation slip systems present. The prediction shares many of the features of the measured full-widths of Figure 11, hence the changes of broadening with viewing angle are likely to be mainly due to variations of slip systems in different orientations. These measurements were also done on rolled samples [3], and it was shown that the change in broadening also showed a good correlation with predictions based on the activity of different slip systems.

The use of the plasticity approach to predict contrast factors, based only on slip anisotropy, works better for low SFE alloys like steel, as shown in [42] or by comparing Figure 11 with Figure 12. But what is interesting is that the approach works for nickel even after large amounts of deformation [3,42]. In alloys with high SFE there is considerable amounts of cross-slip and recovery, which leads to dislocation structures like those shown in Figure 13 to develop. Although, it may be expected that this recovery process would remove most of the mobile dislocations that are predicted by the crystal plasticity models to accommodate the imposed loads, these plots of broadening with angle suggest that this is not the case.
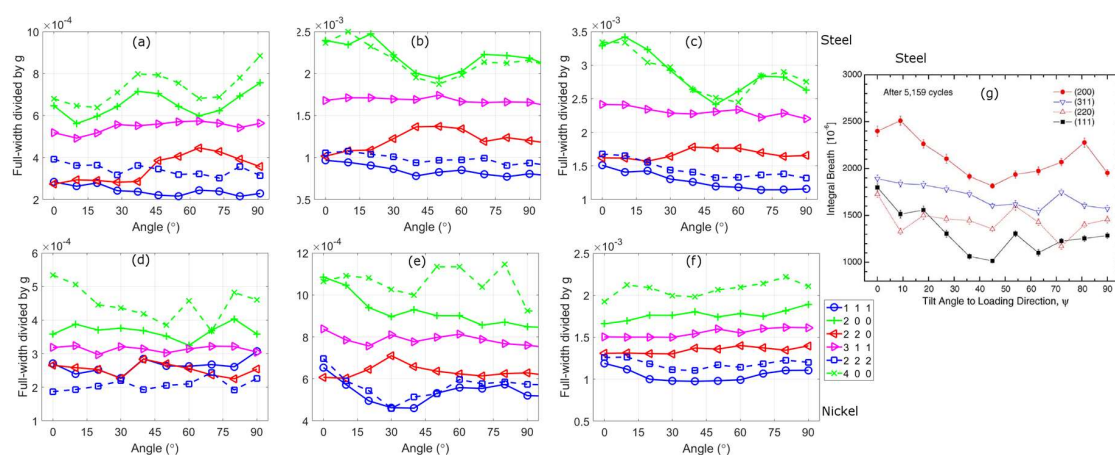

Figure 11. The measured full-width divided by *g* of a stainless steel (**a**–**c**) and nickel alloy (**d**–**f**) after compression testing, at different angles between the compression direction and the diffraction vector [3,42]. The figures are at increasing applied strain. For stainless steel the figures are at (**a**) 2%, (**b**) 10%, and (**c**) 16% applied strain. For nickel, the figures are at (**a**) 2%, (**b**) 10%, and (**c**) 30% applied strain. In (**g**) the integral breadth divided by *g* of a stainless steel alloy after fatigue testing, at angles between the tensile and diffraction vector [27]. The instrumental broadening has been subtracted from the measured values. In (**g**) are changes in the integral breadth (a function of FW and the shape of the tail of the peak) of a stainless steel after fatigue testing taken from Wang et al. [27].
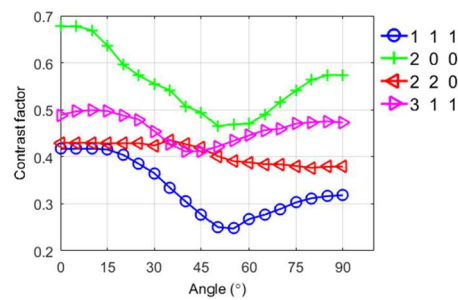
Figure 12. The predicted change in contrast factor for angles between compression and diffraction vectors using a Taylor model. Adapted from [42].

It has been observed by detailed TEM that the dislocation structure can vary significantly with orientations [70,71]. However, to be able to separate the slip anisotropy effect from other changes in DPPA methods, such as the dislocation structure, is difficult. This is partly because it is the product of the dislocation density and the contrast factor that is obtained by DPPA methods. But also due to practical and mathematical limitations of DPPA methods [4,5], such as: each method can give a slightly different results, limitations of separating size and strain components, along with the ambiguity of the parameters that are obtained, such as crystal size. A popular approach to take is to obtain the contrast factor from a crystal plasticity model and then calculate the dislocation density, and other parameters such as crystal size, using this value of the contrast factor. This was the approach taken by Guiglionda et al. [44], who obtained values of the dislocation density for different texture components which changed by a factor of 2 in an aluminium alloy. In their approach the edge to screw ratio was assumed to be 50:50 and no account was taken of dislocations interactions, i.e., all dislocations were assumed to be given by the Orowan equation (Equation (6)). But these assumptions need not be the case, and as shown by Simm et al. [42] can have a large influence on the calculated contrast factors. In their work Simm et al., using the data shown in Figure 11 showed that the difference between the broadening anisotropy of stainless steel and nickel can be described by nickel having: (1) a greater amount of edge dislocations, (2) less mobile dislocations or more cross-slip, and (3) a variation in dislocation density based on the Taylor factor, of up to ~10% in different orientations, which is not found for steel samples. These differences are consistent with differences that may be expected between the alloys. However, the approach does not fully address the cause of the broadening anisotropy because of its simplicity. A more comprehensive approach would instead incorporate more detailed models of work-hardening, along with more detailed descriptions of how different dislocation arrangements contribute to peak profiles, such as is being developed by Bertin and Cai [55].
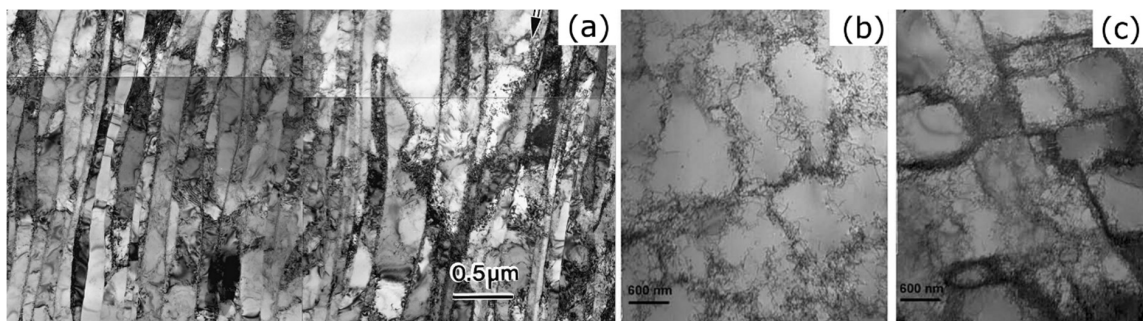
Figure 13. High purity polycrystalline nickel cold rolled to a cold reduction of 95% (**a**). Adapted from Hughes and Hansen [72]. High purity polycrystalline nickel deformed by uniaxial tension to (**b**) 10% and (**c**) 18% applied strain. Adapted from Keller et al. [59].

There are two important implication of broadening anisotropy in different orientations due to slip anisotropy. They can introduce errors in the results of DPPA and they limit the use of DPPA with other techniques.

If the correct value of the contrast factor is not used, because for example slip anisotropy is not accounted for, this can introduce errors in the results of DPPA methods. The potential contribution of this error was assessed in [42] by performing a Warren-Averbach analysis on diffraction patterns obtained at different angles between the tensile and diffraction vectors from the deformed nickel and stainless steel samples discussed previously. The analysis was done using different orders of the same diffraction peak for the 111/222 and 200/400 peaks separately. It was found that the dislocation density fell by ~50%, for both 111/22 and 200/400 analyses, from the values found when the diffraction vector and compression direction were parallel to each other to those found when they were perpendicular. The magnitude of these changes in dislocation density, and the overall trends, were consistent with the predicted changes in the contrast factor calculated by the plasticity approach, due only to slip anisotropy. In addition, the crystal size increased by ~40% with the fall in dislocation density, which may be due to the difficulty in separating size and strain components in the Warren-Averbach approach [5]. Therefore, the possible errors to the results of DPPA by incorrect calculation of the contrast factor are significant. The problem is that in many cases the active slip systems are not known. Even when the imposed deformation is known, limitations in crystal plasticity models and difficulties in relating the model to dislocations, means there will always be an uncertainty in knowing the actual average contrast factor.

A second implication of broadening anisotropy, is it limits the use of DPPA with other techniques. The average value of the broadening of a sample, or dislocation density and crystal size, can be related to other techniques. For example, TEM measurements [73] and positron annihilation spectroscopy [74], can provide dislocation density values to compare with those by DPPA [4,75]. However, broadening anisotropy does limit the use of DPPA alongside other techniques in quantifying differences in the microstructure in different orientations. These differences are crucial to be able to understand plastic deformation in general, and to verify or otherwise plasticity models, as well as to understand the kinetics of recrystallization [76–78] and failure [79,80] of a material.

A diffraction peak represents a fraction of the crystals within a sample based on their orientations. Hence, different diffraction peaks give information about different groups of orientations. This can be seen from the inverse pole figure plots in Figure 14 for the transverse and axial peaks of an untextured FCC alloy. Broadening anisotropy with g, and the difficulty in quantifying it, means that different diffraction peaks (such as 111 and 200) cannot be compared directly to provide the quantity of different defects in different orientations. In addition, because of the changes in the full-width of a given diffraction peak (e.g., 111) with viewing angle (such as shown in Figure 11), are largely due to changes in the contrast factor, it is difficult to even compare the same diffraction peak measured in different directions relative to the sample. This was highlighted by Das et al. [81] (Figure 15) who considered the change in shear strain by digital image correlation, grain orientation spread by EBSD, and the width of diffraction peaks from neutron diffraction, of a metastable austenitic stainless steel. The orientation spread and shear strain values for different grains families with 111, 200, 220, 311 plane normals parallel to the axial and transverse direction can be compared with each other. But the same comparison cannot be done for the integral breadth. For example, it can be said that the shear strain is on average higher in grains with 220 plane normals parallel to the tensile direction, than the other orientation groups. But the broadening of 111, 200 and 220 peaks cannot be compared directly because of broadening anisotropy with g. In addition, the broadening anisotropy with viewing angle, complicates comparison of assessing the broadening of a particular peak in the axial and transverse directions. That is the lower expected contrast factor for transverse peaks compared to axial peaks (i.e., 0° and 90° in Figure 12), mean that more broadening in the axial direction are not necessarily due to differences in dislocation density, but could be due to differences in contrast factor.
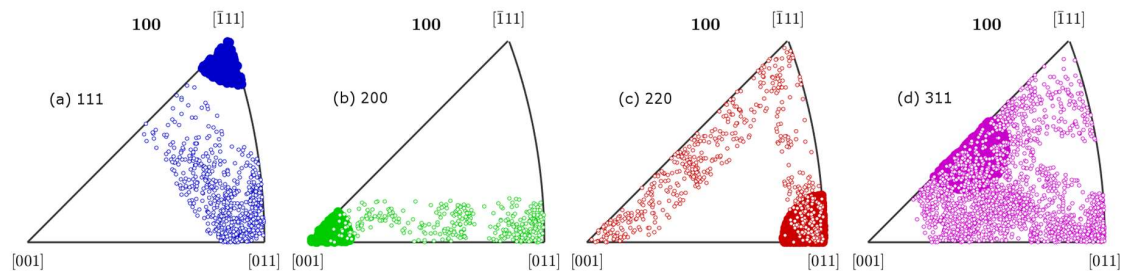
Figure 14. Inverse pole figure (IPF) plots to represent the different orientations given by diffraction peaks in the axial (full-circles) and transverse (empty circles) directions. (**a**) 111 peak, (**b**) 200 peak, (**c**) 220 peak, and (**d**) 311 peak. Where the IPF plots are with reference to the axial direction ([100]) and use a random orientation distribution of 14,000 grains. Note that if the refence was the transverse direction ([001]), the figure would look the same but the icons would be reversed (empty circles would become full circles and vice versa). Calculated using MTEX [82].
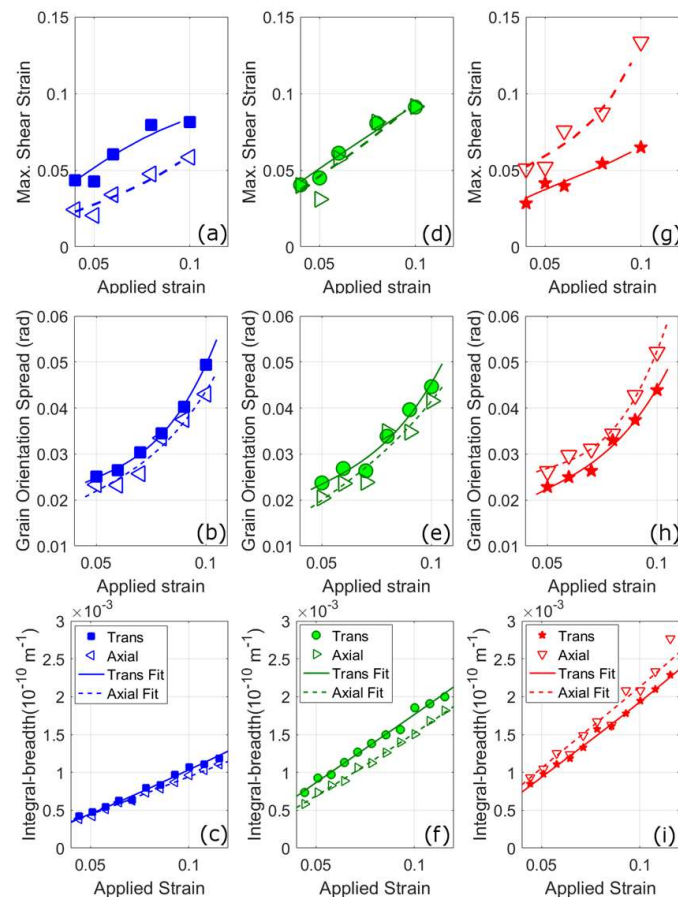
Figure 15. In situ measurements of the maximum shear strain, measured by digital image correlation in an SEM (**a**,**d**,**g**), grain orientation spread, measured by EBSD, (**b**,**e**,**h**), and integral breadth of diffraction peaks, measured using neutron diffraction at ENGIN-X, ISIS, Oxfordshire (**c**,**f**,**i**). The quantities are measured during tensile tests and plotted against applied strain. In (**a**–**c**) are orientations that contribute to the 111 diffraction peak, in (**d**–**f**) the 200 diffraction peak, and in (**g**–**i**) the 220 diffraction peak. Adapted from Das et al. [81].

3.2. Hexagonal Close Packed Alloys

3.2.1. Homogeneous Approach

The issue of peak broadening anisotropy is further complicated in hexagonal close packed (HCP) alloys (such as titanium, zirconium, magnesium), relative to cubic alloys. This is partly a practical issue due to the increased number of different slip systems, but also a result of the variations in the ease in the activity of these different slip systems [57,83,84]. For example, whereas in FCC alloys there is one slip system type {111} [110], in HCP alloys there are several active slip system types. In HCP alloys there are slip systems with both different Burgers vectors (<a> and <c+a>), and different slip planes (basal, prismatic and pyramidal). The homogeneous approach, as outlined by Dragomir and Ungar [30] and based on Equation (3), has been used in a number of works to evaluate the slip activity of different Burgers vector types [85–92]. However, because of the difficulty in quantifying the dislocation types in HCP alloys, corroborating characterisation test results to verify the approach is problematic.

The homogeneous approach in HCP alloys is based on their being a relationship between x (where x is 0 for the prismatic plane and a maximum for the basal plane) and the full-width. By combining Equation (1) with Equation (3), and assuming that crystal size broadening can be ignored and rearranging, the following equation is found:

$$\left(\frac{FW_{hkl}}{g}\right)^2 \approx f_m \rho \left\{ \overline{C_{hk.0}} \left(1 + q_1 x + q_2 x^2 \right) \right\},\tag{9}$$

where $x = \frac{2l^2}{3(ga)^2}$ and $f_M^2 = b^2 \left\{ a_0 \ln(M+1) + b_0 (\ln(M+1))^2 + c_0 (\ln(M+1))^3 + d_0 (\ln(M+1))^4 \right\}$.

A similar approximation can be done for the Warren-Averbach method [23], a DPPA method that uses the Fourier coefficients (A_L) of a peak at different values of the Fourier length (L). The Warren-Averbach equation can be expressed in terms [4] of dislocations, with a density ρ, by the following equation:

$$\ln A_L = \ln A_L^S - \rho g^2 B \overline{C} L^2 f_{Wilk},$$

if size broadening is negligible $\ln A_L^S$ will be close to zero, hence:

$$-\frac{\ln A_L^S}{g^2} \approx \rho B L^2 f_{Wilk}(\overline{C}),\tag{10}$$

where $B = \pi b^2 / 2$, b being the magnitude of the Burgers vector of dislocations, f_{Wilk} the Wilkens function [93], and $\overline{C}$ the average contrast factor.

Hence from Equations (9) and (10) it may be expected that $(FW_{hkl}/g)^2$, $(\beta_{hkl}/g)^2$ (since full-width and integral breadth can be interchanged in the Williamson-Hall equation), and $-\ln A_L^S/g^2$ should change smoothly with x. For this to be the case we are assuming that: the Williamson-Hall and Warren-Averbach equations used are valid, and there is minimal size broadening. This is in general what is found for Ti-6Al-4V deformed by uni-axial tension to different strains, using the full-widths (Figure 16a), the integral breadths (Figure 16b), and the Fourier coefficients (Figure 17). Hence, this gives justification for the use of these equations and the assumption of minimal size broadening. Another feature that is evident from comparing the different figures is that for a given sample, the same changes are observed in $(FW_{hkl}/g)^2$, $(\beta_{hkl}/g)^2$, and $-\ln A_L^S/g^2$. For example, at low strains both $(FW_{hkl}/g)^2$, $(\beta_{hkl}/g)^2$ fall gradually with x, but at higher strains fall then increase, and for a given strain change in a similar manner. Although, the changes of $-\ln A_L^S/g^2$ vary somewhat with the Fourier length, they are comparable to the changes of the full-width or integral breadth of the 5% sample. Therefore, even though, as noted in Section 2.1, the Williamson-Hall method can be problematic for quantitative analysis of broadening anisotropy and the full-width is not the best measure for dislocation broadening [21], the use of the full-width through the Williamson-Hall

method provides a similar description of broadening anisotropy to using integral breadths or Fourier coefficients for this alloy. This gives a justification for the common use of the full-width to describe broadening anisotropy.
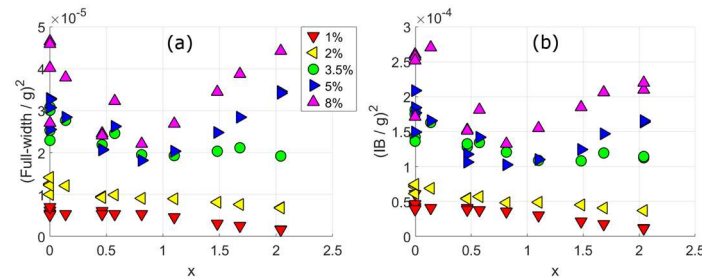
Figure 16. Uni-axial tensile tested Ti-6Al-4V samples measured at 90° between tensile and diffraction vector (the transverse direction), adapted from Simm et al. [42]. In (**a**) are plots of $(FW/g)^2$ against x at different applied strains, where FW is the full-width. In (**b**) are plots of $(IB/g)^2$ against x at different applied strains, where IB is the integral breadth.
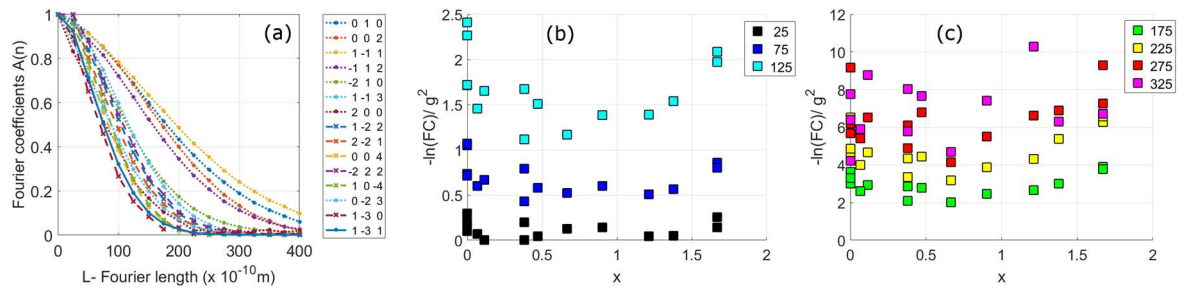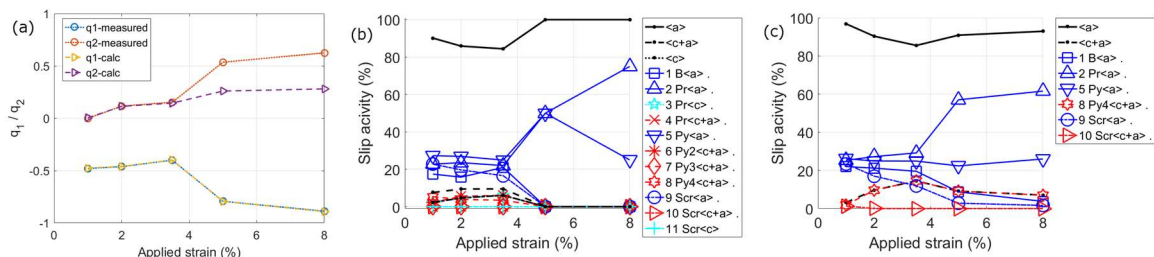

Figure 17. Uni-axial tensile tested Ti-6Al-4V sample measured at 90° between tensile and diffraction vector (the transverse direction) after 5% applied strain, this is the same data shown in Figure 16. In (**a**) the physically broadened Fourier coefficients (A_L) plotted against the Fourier length. In (**b**,**c**) are plots of $-ln(A_L)/g^2$ against x for different Fourier lengths (given in legend in units of 10^{-10} m) for the first 15 HCP diffraction peaks.

From the changes in full-width, or integral breadth, shown in Figure 16 the following trends are observed. Up to a strain of 3.5% the $(FW/g)^2$ falls almost linearly with x. Whereas for higher strains there is a bigger fall in $(FW/g)^2$ at low x, followed by an increase after $x > 1$. From Equation (9) this would be interpreted as $q_1 < 0$ and $q_2 \sim 0$ for samples up to 3.5%, and at higher strains $q_1 < 0$, but lower than q_1 at lower strains, and $q_2 > 0$. Which is what is found from fits to a modified Williamson-Hall equation, as shown in Figure 18b.

In Figure 18c,d these q values have been used to determine the slip activity, using two slightly different approaches. The first approach (Figure 18c) uses a similar approach to Dragomir and Ungar [30]. The second approach (Figure 18d) is a slight modification to the previous one, whereby the available slip system types are reduced to those expected to be the most important types in titanium [83]. This type of approach, involving reducing the available slip systems has been used by different authors [31,85]. These approaches are generally only used to predict the quantity of different Burgers vector types, <a>, <c+a> and <c>; although Mathis et al. [85] also used the approach to find the relative quantity of two different slip system types, prismatic and basal <a>. The reason for this is that using two variables (q_1 and q_2) to find details of any more than three parameters is impractical because there are too many possible combinations. However, looking at the contributions to calculated values is useful to understand the contributions to the calculated <a>, <c+a> and <c> values. Figure 18 shows that <a> type dislocations dominate for both approaches and across all applied strains. Furthermore, when the individual slip system types are considered prismatic <a> is the most active slip system

type (this is because prismatic <a> and pyramidal <a> are the only slip system types with $q_1 < 0$ and $q_2 > 0$, with prismatic <a> having q values with larger magnitude). This may be expected given that <a> dislocations are much easier to activate than those with a c-component; furthermore <c> dislocations which are the hardest to activate have the lowest percentage. However, given that <a> slip does not satisfy the von Mises criterion of needing at least five independent slip systems for homogenous plastic deformation of a polycrystal [62], more dislocations with a c-component would be expected. This could be accounted for by some grains deforming more than others in a systematic way, but would go against the assumption in the Homogeneous approach that all grains are the same. There is another problem with the approaches prediction of almost 100% <a> dislocations to explain the shape of FW against x. This is the increase in broadening at high x which cannot be explained by <a> dislocations that have vanishing contrast at high x values (Figure 3).

Figure 18. Uni-axial tensile tested Ti-6Al-4V samples measured at 90° between tensile and diffraction vector (the transverse direction), adapted from Simm et al [42]. In (**a**) are the fitted q values using a modified Williamson-Hall equation and the full-width values from Figure 16a. The calculated q values from the slip systems in (**c**) are also shown. In (**b**,**c**) are calculated activities of different slip system types, see Simm [3]. The method in (**b**) is similar to that of Dragomir and Ungar [30], whereas in (**c**) the available slip system types have been reduced to those expected in Ti-6Al-4V.

The choice of these slip systems from the q values also influences the dislocation density. This is not the case in cubic crystals since the value of $b^2 C_{h00}$ varies very little between edge and screw dislocations. However, for HCP alloys the value of $b^2 C_{hk.0}$ can vary significantly between different slip system types as shown in Figure 3 and Table 1. Hence, because of the relationship in DPPA methods between the dislocation density and the contrast factor (as shown in Equation (1)), the choice of slip systems can have a large effect on the dislocation density obtained. To obtain the dislocation density it is first necessary to obtain a value for the average $b^2 C_{hk.0}$ based on the expected slip systems present. $\overline{b^2 C_{hk.0}}$ can be found in several ways including by averaging over the dislocation types (<a>, <c+a> and <c>) (Equation (11)), or the slip system types (the 11 slip system types in Figure 3) (Equation (12)). Where $\overline{C_i^{disloc.}}$ is the average contrast factor for the <a>, <c+a> and <a> dislocations, using the averaged contrast factor values of the different slip system types $\overline{C_i^{slipsys}}$ shown in Figure 3.

$$\overline{b^2 C_{hk.0}} = \sum_i^3 b_i^2 \overline{C_i^{disloc.}}, \tag{11}$$

$$\overline{b^2 C_{hk.0}} = \sum_i^{11} b_i^2 \overline{C_i^{slipsys}}, \tag{12}$$

Using the slip system activities shown in Figure 18c,d and Equations (11) and (12), the values of $\overline{b^2 C_{hk.0}}$ shown in Figure 19 were calculated. These different values vary by as much as 30% with applied deformation for a particular methodology, and the values from the different methodologies can vary by up to 80%. In general, the 'All disloc. avg.' method is used in research papers, which uses all slip systems and Equation (11). But there are problems with this due to the averaging of Equation (11), because it is unlikely that all slip system types defined in Table 1 exist in the same quantity (e.g., in magnesium alloys a greater proportion of basal <a> dislocations would be expected than in a titanium alloy). However, the use of Equation (12) is also problematic as it is unlikely that the

individual slip system types can be obtained from the two *q* values. Any method to determine $\overline{b^2 C_{hk.0}}$ is fraught with potential errors, therefore it may be advantageous to assume a constant value of $\overline{b^2 C_{hk.0}}$ for a particular set of data, unless a good justification for doing otherwise can be established.
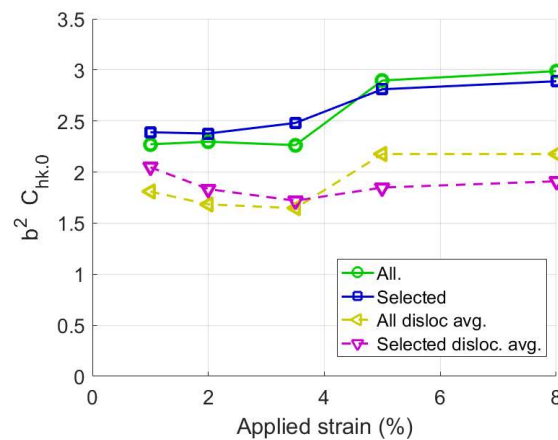
Figure 19. Changes in $\overline{b^2 C_{hk.0}}$ (since *b* varies with slip system) from the slip activities determined in Figure 18, for Ti-6Al-4V deformed by uni-axial tension to various strains. The results labelled 'All' use the slip activities in Figure 18c using all slip system types, and labelled 'Selected' use the slip activities in Figure 18d which use selected slip system types. Those labelled 'disloc. avg.' take the average values of the different dislocation types (<a>, <c+a> and <c>), whereas those without sum up the individual slip system types.

3.2.2. Plasticity Approach

In Figure 20 are full-width divided by *g* plots at different angles between the compression/tension direction and the diffraction vector, for a zirconium alloy (a) and a magnesium alloy (b) (taken from [94]). The figure shows, in the same way as seen with the FCC samples, that the full-width of a diffraction peak can vary considerably at different angles. These differences show that the assumptions used in the homogeneous approach, that all grains deform in the same way, is not valid. To examine how this would influence the use of the homogeneous approach it is worth considering the change in full-width with *x*.

In Figure 21a–c are plots of the change in full-width with *x* for three different HCP alloys for axial and transverse orientations: in (a) a titanium alloy [42], (b) a magnesium alloy [94], and (c) a zirconium alloy [94]. In the figure the angle between tensile axis and diffraction vector is 0° for the axial direction and 90° for the transverse. The changes of *FW/g* with *x* are similar for the zirconium alloy and Ti-6Al-4V. The alloys also both display a marked difference in the change in *FW/g* with *x* in the two measurement directions. Whereas, for the magnesium alloy there is very little difference in the two measurement directions, with a change in *FW/g* that is similar to that found for titanium and zirconium alloys in the axial direction. In Figure 21d are plots of *FW/g* against *x* for a deformed magnesium alloy (from Mathis et al. [85]) and a deformed zirconium alloy (from Long et al. [91]). The magnesium alloy is measured in the transverse direction and the zirconium alloy at an angle between transverse and axial directions. In general, the changes of *FW/g* with *x* for the zirconium alloys is similar to that of the titanium and zirconium alloys shown in Figure 21a,c and the magnesium alloy is slightly different and similar to that of the magnesium alloy shown in Figure 21b.

In general, in HCP alloys with a lower c/a ratio, such as titanium and zirconium alloys, will deform preferentially by prismatic <a> slip. Whereas, those with a higher c/a ratio, such as magnesium and cobalt alloys, will deform preferentially by basal <a> slip. Hence, the similarities in broadening anisotropy between zirconium and titanium alloys, and their difference with the broadening anisotropy of magnesium alloys may be expected. To examine these differences, it is

worthwhile to consider how the activity of different slip system types can vary in the different alloys and in different orientations.
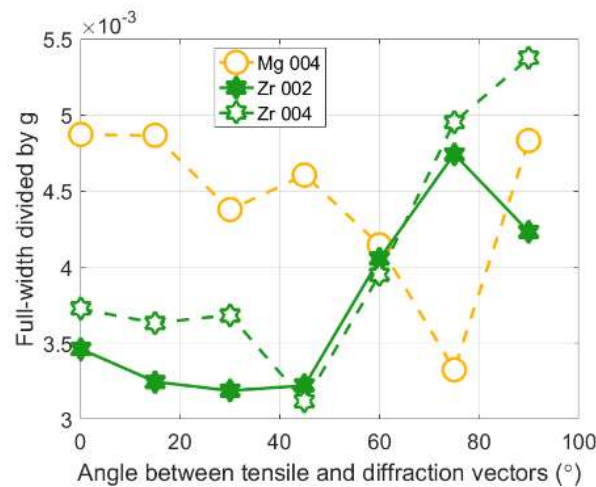
Figure 20. The change in 0002/0004 full-width with angle between the tensile/compression direction and the diffraction vector, for a magnesium alloy and a zirconium alloy. Adapted from Simm et al. [94].
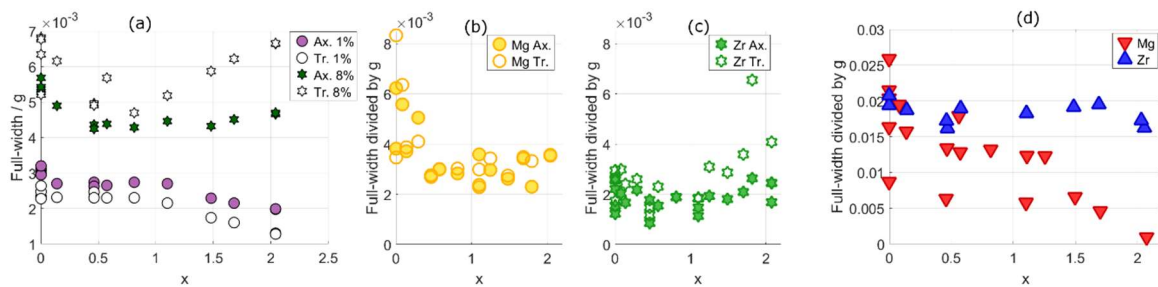

Figure 21. The change in full-width divided by *g* with *x* for different HCP alloys. In (**a**) a titanium alloy (Ti-6Al-4V) deformed in tension to strains 1% and 8% in the axial and transverse directions. In (**b**, **c**) measurements at HRPD on a magnesium alloy compressed to 7% (**b**) and a zirconium alloy deformed in tension to 5% (**c**) (data in b and c taken from Simm et al. [94]). In (**d**) a zirconium alloy deformed to 5% by compression and measured at an angle of $\pm 32°$ between the transverse direction and the diffraction vector (data taken from Long et al. [91]), and a magnesium alloy deformed to 6% by compression measured in the transverse direction (data taken from Mathis et al. [85]).

There is an increased difficulty in predicting the deformation and activity of different slip systems in HCP alloys compared to cubic alloys [52,95]. This is due the greater number of slip systems that can be active and the variations in their ease of activity. The shear stress needed to activate different slip system types varies considerably, known as the critically resolved shear stress (CRSS), for different slip systems [57,84,96]. Those systems with a <c> component are much harder to activate than the <a> slip system types, and certain <a> slip system types are preferred in different alloys. In addition to this, deformation twinning is an important mode of deformation in HCP alloys [95,97]. The result of this is that deformation is more heterogeneous in HCP alloys [98–100], where different grains or orientations can have markedly different deformation microstructures. The most successful models to predict the slip systems and changes during deformation are crystal plasticity finite element models [51] and viscoplastic self-consistent models [52]. The simpler use of the Schmid factor to quantify slip activity has however shown some success in understanding the deformation of HCP alloys [101–104]. The Schmid factor can help to quantify what slip systems may be likely to be active in different

orientations. The higher the value of the Schmid factor multiplied by the CRSS of a slip system, the more likely it is to be active.

In Figure 22a and b are plots of the change in Schmid factor with x for the most important slip system types in HCP alloys [84]. The figure shows that there are large changes in the Schmid factor with x, and the changes are different for the different slip system types and measurement directions. For example, prismatic <a> slip is more likely to be activated when the normal of the prismatic plane is parallel to the tensile direction ($x = 0$ in axial plot, or $x\sim2$ in the transverse plot), and less likely when the normal of the basal plane is parallel to the tensile direction ($x\sim2$ in axial plot, or $x = 0$ in transverse plot).
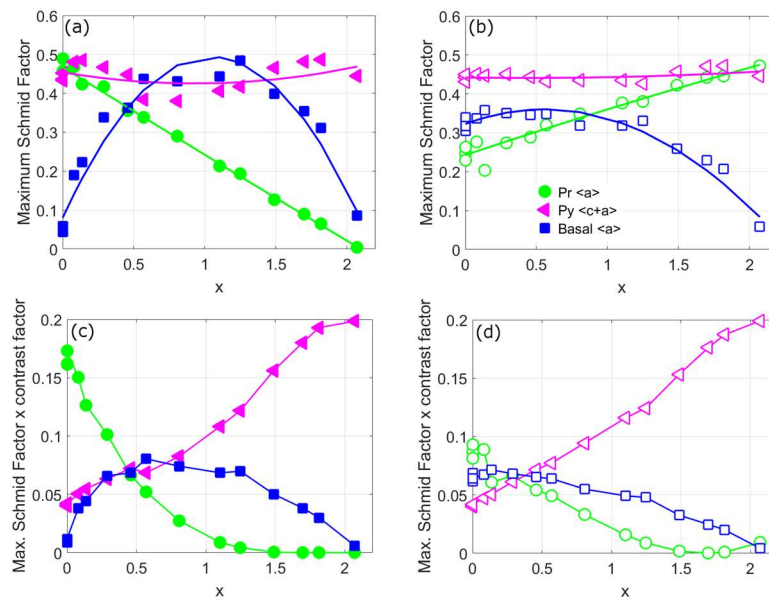
Figure 22. The maximum Schmid factor of different slip system types at different angles of x, for the axial (**a**) and transverse directions (**b**). And the average contrast factor multiplied by the maximum Schmid factor, for axial (**c**) and transverse directions (**d**). The slip systems are those expected to be most important in HCP alloys, prismatic <a> (Pr <a> in green), pyramidal <c+a> (Py <c+a> in pink) and basal <a> (Basa l<a> in blue).

To get an indication of how these predicted changes in slip activity would influence the broadening, the Schmid factors are multiplied by the contrast factors values at different values of x (Figure 22c,d). This is done for each of the different slip system types using the maximum Schmid factor and the average edge contrast factors values at different values of x (from [30]). Both of these approximations, the use of the maximum Schmid factor and the average contrast factor values, doesn't significantly affect the overall trends as shown in Simm et al. [42]. There are two observations from Figure 22c,d that are of particular interest regarding the broadening anisotropy of the alloys shown in Figure 21. Firstly, in these plots the difference in the two measurement directions is much smaller than that seen for the contrast factors. Secondly, basal <a> has a higher value at $x > 1$ than prismatic <a>, and hence should contribute more to broadening at $x > 1$. These changes go against the broadening differences observed: (a) between alloys that deform principally by basal (magnesium alloys) and prismatic (titanium and zirconium alloys) slip, and (b) between broadening in the axial and transverse directions observed in alloys that deform principally by prismatic slip. With regards to (a), from Figure 21 the full-width of magnesium alloy tends to fall more with x than seen for zirconium and titanium alloys. But this is the opposite of what is expected from the predictions in Figure 22c,d. Whereas, with regards to (b), the expected broadening from prismatic <a> slip falls to zero with increasing x in both directions. Hence, the dominant slip system is unable to explain the

difference in broadening anisotropy in the two directions and the increased broadening seen in the transverse direction at increasing x. Both observations point to an unusually high broadening for alloys that preferentially deform by prismatic <a> slip in the transverse direction at high values of x. From Figure 22b it can be seen that for these orientations there is a high expected amount of prismatic <a> slip relative to the axial direction, in contrast to basal <a> or pyramidal <c+a> slip which have similar behaviour in the transverse and axial directions with x. However, because these prismatic <a> dislocations have a diminishing contrast factor (see Figure 3), they are not expected to contribute to broadening. If these dislocations were to contribute to broadening in a way that is not related to the contrast factor, a 'non-contrast factor' broadening, this could explain the discrepancies observed. The presence of these dislocations may break up the grains into domains that don't diffract coherently, providing an additional crystal size broadening. Although, the activity of different slip systems will be more complicated than given by the Schmid factors, the discussion using the Schmid factors is able to provide an explanation for the unusual broadening anisotropy observed in the HCP alloys. This 'non-contrast factor' broadening has important implications on how broadening anisotropy is dealt with in HCP alloys, and on the underlying assumption used that variations in contrast factor alone can explain broadening anisotropy.

The analysis presented in this section highlights problems in using the homogeneous approach to explain broadening anisotropy in HCP alloys. These issues place doubt on the use of the homogeneous approach for deformed HCP alloys, particularly to quantify slip activity. If broadening anisotropy is not properly accounted for there are significant potential errors that can result from DPPA methods, which are much larger than would be for cubic alloys. However, the solution to this problem is not clear and hence it may therefore be best practice to assume a constant value of $\overline{b^2 C_{hk.0}}$ when comparing different samples. Further investigation is needed as the implications of the analysis of HCP alloys, and the significance of 'non-contrast factor' broadening, has important implications for DPPA methods in HCP alloys.

3.2.3. Twinning

To examine the effect of twinning on peak profiles two different titanium alloys are compared: Ti-6Al-4V and a commercially pure titanium (Ti-CP). Both alloys were deformed by uni-axial tension to a range of applied strains and measured by synchrotron x-ray diffraction, at ID31, ESF, Grenoble (more details in [3,42]). Whereas, Ti-CP is known to display marked deformation twinning [65,103,105,106], in Ti-6Al-4V twinning is rarely found [63,64,107]. Although, there will be more differences between the alloys than just twinning, because even the ability of an alloy to twin will influence the activity of the different slip systems, it is worth considering the broadening of the two alloys.

In Figure 23 are the changes in the shape of diffraction peaks of the two alloys with x; including the change in *FW/g*, the shape of the tails of the peaks (given by the pseudo-Voigt mixing parameter [108]) and broadening anisotropy (the difference in FW on the left and right side of the peak). The change in the shape of the peaks with x shares similarities for the two alloys. Both have a transverse *FW/g* that falls then increases with x, and have higher value at high x in the transverse direction than the corresponding axial *FW/g*. The *FW/g* values in the axial direction are different for both alloys, with *FW/g* being more constant with x for Ti-CP than for Ti-6Al-4V, although the differences are less evident at the other measured strains of Ti-6Al-4V [3]. In addition, the shape of the tails of the peaks and the peak's asymmetry has similarities for the two alloys. The pseudo-Voigt mixing parameter of both alloys increases with x for the axial direction, and falls with x for the transverse direction. The asymmetry parameter is approximately constant with x for both alloys. The work of Balogh, Tichy and Ungar [40] on how twinning would contribute to diffraction profiles in HCP alloys, shows that twin boundaries cause changes in the broadening and asymmetry of a peak. However, the results suggest the broadening and asymmetry of peaks to be similar in both alloys. This suggests that the contribution of twinning to broadening anisotropy in HCP alloys is minimal. However, twinning will also affect the activity of different slip systems and in turn broadening anisotropy,

so further work is needed to understand how twins contribute to broadening. Twins in HCP alloys are most often of the order of several micrometres in thickness [62,109], rather than the deformation twins observed in FCC alloys which tend to be fractions of micrometres in thickness [66,110,111] (as shown in Figure 24). Therefore, in HCP alloys the number of twin boundaries can be low even though the volume of twinned grains can be large. In addition, there can be many other reasons that a twin could causes broadening. These include variations in the intergranular strains in twins compared to un-twinned regions, that contribute to a diffraction peak [95,112]. Along with the dislocations present in the twin before the twinning has occurred. Hence, these factors, are probably more important considerations to quantify twinning in HCP alloys, than the traditional methods (e.g., Balogh et al. [40]) that are based on the ordering of atoms at the twin boundary.
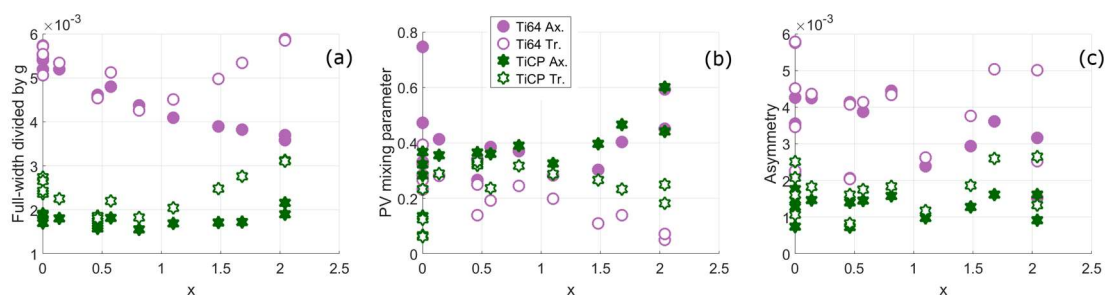
Figure 23. The change in peak-shape of Ti-6Al-4V and Ti-CP with *x*, for the axial and transverse directions. Before alloys were deformed by uni-axial tension, Ti-6Al-4V is deformed to 5% applied strain and Ti-CP to 3.5% applied strain. In (**a**) the changes in full-width, in (**b**) the changes of the pseudo-Voigt mixing parameter, and in (**c**) changes in the asymmetry of the peaks. Adapted from Simm et al. [42].
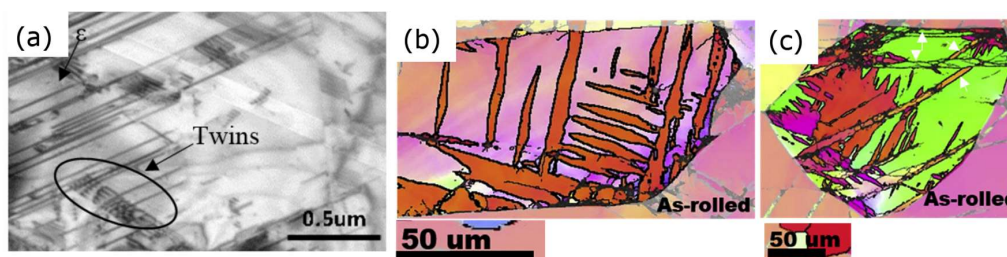
Figure 24. Deformation twins. Left (**a**) from a stainless steel alloy (adapted from [110]) and right (**b**,**c**) from a magnesium alloy (adapted from [109]).

4. Conclusions

Diffraction peak profile analysis (DPPA) is a valuable technique for science, engineering and applied physics communities to characterise the nano-structure of crystalline materials that is not possible or not easy by other techniques.

Formulism to describe broadening anisotropy, such as those given for the contrast factor and planar faults, are valuable for quantifying details of the microstructure such as the relative amount of different dislocation types, or the quantity of planar faults. In addition, their use can improve the statistics for analysis. This is achieved by allowing the use of many more diffraction peaks which represent a higher fraction of the sample, than possible by using multiple orders of the same peak.

However, there are problems with using these formalisms, which are a result of the heterogeneous nature of plastic deformation, and the practical and mathematical limitations of peak profile methods. They add errors to the results from DPPA methods. This is most evident for slip system and planar fault predictions which are used to describe broadening anisotropy. But other results such as dislocation

density and crystal size will also be affected. These errors will be larger for HCP alloys due to the greater number of slip systems and differences in their ease of activity.

It is suggested that a way to retain the benefits of using the formulae to describe planar faults is by using the broadening and peak shifts of different orders of the same peak. However, a way to be able to quantify the dislocation slip system types present (i.e., edge and screw, or <a> and <c+a>) in a sample is more complicated. This is particularly the case in HCP alloys were it is shown that significant broadening anisotropy can result from 'non contrast factor' broadening. Which goes against current formalisms that assume that all broadening anisotropy is due to the contrast factor.

There are several implications of broadening anisotropy on the results of diffraction peak profile analysis methods:

(1)　They add errors to the results obtained by DPPA methods.
(2)　They limit the ability of DPPA methods to be used with other characterisation techniques. But,
(3)　They can be used to provide additional information about the materials deformation microstructure.
(4)　They offer a means to develop and verify models of plastic deformation that incorporate crystal plasticity formulations with work-hardening models that predict changes that occur at the scale of dislocations.

Conflicts of Interest: The authors declare no conflict of interest.

References

1.　Warren, B.E. *X-ray Diffraction*; Addison-Wesley Publishing Co.: Reading, UK, 1969.
2.　Kuzel, R. Dislocation line broadening. *Zeitschrift Fur Kristallographie* **2006**, *1*, 75–80. [CrossRef]
3.　Simm, T.H. The Use of Diffraction Peak Profile Analysis in Studying the Plastic Deformation of Metals. Ph.D. Thesis, University of Manchester, Manchester, UK, 2012.
4.　Simm, T.H.H.; Withers, P.J.; da Fonseca, J.Q. An evaluation of diffraction peak profile analysis (DPPA) methods to study plastically deformed metals. *Mater. Des.* **2016**, *111*, 331–343. [CrossRef]
5.　Van Berkum, J.G.M.; Vermeulen, A.C.; Delhez, R.; de Keijser, T.H.; Mittemeijer, E.J. Applicabilities of the Warren-Averbach analysis and an alternative analysis for separation of size and strain broadening. *J. Appl. Crystallogr.* **1994**, *27*, 345–357. [CrossRef]
6.　Rietveld, H.M. A profile refinement method for nuclear and magnetic structures. *J. Appl. Crystallogr.* **1969**, *2*, 65–71. [CrossRef]
7.　Le Bail, A. Modelling anisotropic crystallite size/microstrain in Rietveld analysis. *NIST Spec. Publ.* **1992**, *846*, 142–153. [CrossRef]
8.　Stokes, A.R.; Wilson, A.J.C. The diffraction of X rays by distorted crystal aggregates—I. *Proc. Phys. Soc.* **1944**, *56*, 174–181. [CrossRef]
9.　Stephens, P.W. Phenomenological model of anisotropic peak broadening in powder diffraction. *J. Appl. Crystallogr.* **1999**, *32*, 281–289. [CrossRef]
10.　Popa, N.C. The (hkl) Dependence of Diffraction-Line Broadening Caused by Strain and Size for all Laue Groups in Rietveld Refinement. *J. Appl. Crystallogr.* **1998**, *31*, 176–180. [CrossRef]
11.　Krivoglaz, M.A. *X-ray and Neutron Diffraction in Nonideal Crystals*; Springer-Verlag: Berlin, Germany, 1996.
12.　Simm, T.H. Supplementary data and analysis for "Peak broadening anisotropy and the contrast factor in metal alloys". *OSF* **2018**. [CrossRef]
13.　Simm, T.H. DPPA BIGdippa and dippaFC. *OSF* **2018**. [CrossRef]
14.　Liu, Q.; Zhao, C.; Su, S.; Li, J.; Xing, Y.; Cheng, B. Strain Field Mapping of Dislocations in a Ge/Si Heterostructure. *PLoS ONE* **2013**, *8*, 4–9. [CrossRef] [PubMed]

15. Dupraz, M.; Beutier, G.; Rodney, D.; Mordehai, D.; Verdier, M. Signature of dislocations and stacking faults of face-centred cubic nanocrystals in coherent X-ray diffraction patterns: A numerical study. *J. Appl. Crystallogr.* **2015**, *48*, 621–644. [CrossRef] [PubMed]

16. Borbély, A.; Dragomir-Cernatescu, J.; Ribárik, G.; Ungár, T.; Borbely, A.; Dragomir-Cernatescu, J.; Ribarik, G.; Ungar, T. Computer program ANIZC for the calculation of diffraction contrast factors of dislocations in elastically anisotropic cubic, hexagonal and trigonal crystals. *J. Appl. Crystallogr.* **2003**, *36*, 160–162. [CrossRef]

17. Armstrong, R.W. Crystal Dislocations. *Crystals* **2016**, *6*, 9. [CrossRef]

18. Williamson, G.K.; Hall, W.H. X-ray line broadening from filed aluminium and wolfram. *Acta Metall.* **1953**, *1*, 22–31. [CrossRef]

19. Ungár, T.; Borbély, A. The effect of dislocation contrast on x-ray line broadening: A new approach to line profile analysis. *Appl. Phys. Lett.* **1996**, *69*, 3173. [CrossRef]

20. Scardi, P.; Leoni, M.; Delhez, R. Line broadening analysis using integral breadth methods: A critical review. *J. Appl. Crystallogr.* **2004**, *37*, 381–390. [CrossRef]

21. Wilkens, M. The determination of density and distribution of dislocations in deformed single crystals from broadened X-ray diffraction profiles. *Phys. Status Solidi* **1970**, *2*, 359–370. [CrossRef]

22. Ungár, T.; Tichy, G. The Effect of Dislocation Contrast on X-Ray Line Profiles in Untextured Polycrystals. *Phys. Status Solidi* **1999**, *171*, 425–434. [CrossRef]

23. Warren, B.E. X-ray studies of deformed metals. *Prog. Met. Phys.* **1959**, *8*, 147–202. [CrossRef]

24. Ungár, T.; Gubicza, J.; Hanak, P.; Alexandrov, I. Densities and character of dislocations and size-distribution of subgrains in deformed metals by X-ray diffraction profile analysis. *Mater. Sci. Eng. A* **2001**, *319–321*, 274–278. [CrossRef]

25. Ungár, T.; Dragomir, I.; Révész, Á.; Borbély, A. The contrast factors of dislocations in cubic crystals: The dislocation model of strain anisotropy in practice. *J. Appl. Crystallogr.* **1999**, *32*, 992–1002. [CrossRef]

26. Abouhilou, F.; Khereddine, A.; Alili, B.; Bradai, D. X-ray peak profile analysis of dislocation type, density and crystallite size distribution in cold deformed Pb-Ca-Sn alloys. *Trans. Nonferr. Met. Soc. China* **2012**, *22*, 604–607. [CrossRef]

27. Wang, X.L.; Wang, Y.D.; Stoica, A.D.; Horton, D.J.; Tian, H.; Liaw, P.K.; Choo, H.; Richardson, J.W.; Maxey, E. Inter- and intragranular stresses in cyclically-deformed 316 stainless steel. *Mater. Sci. Eng. A* **2005**, *399*, 114–119. [CrossRef]

28. Ungár, T.; Ott, S.; Sanders, P.; Borbély, A.; Weertman, J. Dislocations, grain size and planar faults in nanostructured copper determined by high resolution X-ray diffraction and a new procedure of peak profile analysis. *Acta Mater.* **1998**, *46*, 3693–3699. [CrossRef]

29. Ungár, T.; Ribárik, G.; Zilahi, G.; Mulay, R.; Lienert, U.; Balogh, L.; Agnew, S.R. Slip systems and dislocation densities in individual grains of polycrystalline aggregates of plastically deformed CoTi and CoZr alloys. *Acta Mater.* **2014**, *71*, 264–282. [CrossRef]

30. Dragomir, I.C.; Ungár, T. Contrast factors of dislocations in the hexagonal crystal system. *J. Appl. Crystallogr.* **2002**, *35*, 556–564. [CrossRef]

31. Seymour, T.; Frankel, P.; Balogh, L.; Ungár, T.; Thompson, S.P.; Jädernäs, D.; Romero, J.; Hallstadius, L.; Daymond, M.R.; Ribárik, G.; et al. Evolution of dislocation structure in neutron irradiated Zircaloy-2 studied by synchrotron x-ray diffraction peak profile analysis. *Acta Mater.* **2017**, *126*, 102–113. [CrossRef]

32. Treacy, M.M.J.; Newsam, J.M.; Deem, M.W. A general recursion method for calculating diffracted intensities from crystals containing planar faults. *Proc. R. Soc. Math. Phys. Sci.* **1991**, *433*, 499–520. [CrossRef]

33. Estevez-Rams, E.; Penton-Madrigal, A.; Lora-Serrano, R.; Martinez-Garcia, J. Direct determination of microstructural parameters from the x-ray diffraction profile of a crystal with stacking faults. *J. Appl. Crystallogr.* **2001**, *34*, 730–736. [CrossRef]

34. Balogh, L.; Ribarik, G.; Ungár, T. Stacking faults and twin boundaries in fcc crystals determined by x-ray diffraction profile analysis. *J. Appl. Phys.* **2006**, *100*, 1–10. [CrossRef]

35. Stokes, A.R.; Wilson, A.J.C.; Bragg, W.L. A method of calculating the integral breadths of Debye-Scherrer lines. *Math. Proc. Camb. Philos. Soc.* **1942**, *38*, 313. [CrossRef]

36. Unga, T.; Gubicza, J.; Riba, G. MWP-fit: A program for multiple whole-profile fitting of diffraction peak profiles by ab initio theoretical functions. *J. Appl. Crystallogr.* **2001**, *34*, 669–676.

37. Scardi, P.; Leoni, M. Fourier modelling of the anisotropic line broadening of X-ray diffraction profiles due to line and plane lattice defects. *J. Appl. Crystallogr.* **1999**, *32*, 671–682. [CrossRef]

38. Ungár, T.; Stoica, A.D.; Tichy, G.; Wang, X.L. Orientation-dependent evolution of the dislocation density in grain populations with different crystallographic orientations relative to the tensile axis in a polycrystalline aggregate of stainless steel. *Acta Mater.* **2014**, *66*, 251–261. [CrossRef]

39. Csiszár, G.; Balogh, L.; Misra, A.; Zhang, X.; Ungár, T. The dislocation density and twin-boundary frequency determined by X-ray peak profile analysis in cold rolled magnetron-sputter deposited nanotwinned copper. *J. Appl. Phys.* **2011**, *110*. [CrossRef]

40. Balogh, L.; Tichy, G.; Ungár, T. Twinning on pyramidal planes in hexagonal close packed crystals determined along with other defects by X-ray line profile analysis. *J. Appl. Crystallogr.* **2009**, *42*, 580–591. [CrossRef]

41. Balogh, L.; Figueiredo, R.B.; Ungár, T.; Langdon, T.G. The contributions of grain size, dislocation density and twinning to the strength of a magnesium alloy processed by ECAP. *Mater. Sci. Eng. A* **2010**, *528*, 533–538. [CrossRef]

42. Simm, T.H.; Withers, P.J.; da Fonseca, J.Q. Peak broadening anisotropy in deformed face-centred cubic and hexagonal close-packed alloys. *J. Appl. Crystallogr.* **2014**, *47*, 1535–1551. [CrossRef]

43. Borbely, A.; Driver, J.H.; Ungár, T. X-ray method for the determination of stored energies in texture components of deformed metals; application to cold worked ultra high purity iron. *Acta Mater.* **2000**, *48*, 2005–2016. [CrossRef]

44. Guiglionda, G.; Borbely, A.; Driver, J.H. Orientation-dependent stored energies in hot deformed Al-2.5%Mg and their influence on recrystallization. *Acta Mater.* **2004**, *52*, 3413–3423. [CrossRef]

45. Bate, P.S.; da Fonseca, J.Q. Texture development in the cold rolling of IF steel. *Mater. Sci. Eng. A* **2004**, *380*, 365–377. [CrossRef]

46. Sevillano, J.G.; van Houtte, P.; Aernoudt, E. Large strain work hardening and textures. *Prog. Mater. Sci.* **1980**, *25*, 69–134. [CrossRef]

47. Honniball, P.D.; Preuss, M.; Rugg, D.; da Fonseca, J.Q. Grain Breakup During Elevated Temperature Deformation of an HCP Metal. *Metall. Mater. Trans. A Phys. Metall. Mater. Sci.* **2015**, *46*, 2143–2156. [CrossRef]

48. Da Fonseca, J.Q.; Oliver, E.C.; Bate, P.S.; Withers, P.J. Evolution of intergranular stresses during in situ straining of IF steel with different grain sizes. *Mater. Sci. Eng. A* **2006**, *437*, 26–32. [CrossRef]

49. Taylor, G.I. The Mechanism of Plastic Deformation of Crystals. Part I. Theoretical. *Proc. R. Soc. A Math. Phys. Eng. Sci.* **1934**, *145*, 362–387. [CrossRef]

50. Kurdjumov, G.; Sachs, G. Over the mechanisms of steel hardening. *Z. Phys.* **1930**, *64*, 325–343.

51. Bate, P. Modelling deformation microstructure with the crystal plasticity finite-element method. *Philos. Trans. R. Soc. A Math. Phys. Eng. Sci.* **1999**, *357*, 1589–1601. [CrossRef]

52. Lebensohn, R.A.; Tomé, C.N. A self-consistent anisotropic approach for the simulation of plastic deformation and texture development of polycrystals: Application to zirconium alloys. *Acta Metall. Mater.* **1993**, *41*, 2611–2624. [CrossRef]

53. Cottrell, A.H. *Dislocations and Plastic Flow in Crystals*; Clarendon Press: London, UK, 1964.

54. Cottrell, A.H. Commentary. A brief view of work hardening. *Dislocations Solids* **2002**. [CrossRef]

55. Bertin, N.; Cai, W. Computation of virtual X-ray diffraction patterns from discrete dislocation structures. *Comput. Mater. Sci.* **2018**, *146*, 268–277. [CrossRef]

56. Bulatov, W.; Cai, V.V. *Computer Simulations of Dislocations*; Oxford University Press: Oxford, UK, 2006. [CrossRef]

57. Hull, D.; Bacon, D.J. *Introduction to Dislocations*; Elsevier Science: New York, NY, USA, 2001.

58. Zehetbauer, M. Cold work hardening in stages IV and V of F.C.C. metals-II. Model fits and physical results. *Acta Metall. Mater.* **1993**, *41*, 589–599. [CrossRef]

59. Keller, C.; Hug, E.; Retoux, R.; Feaugas, X. TEM study of dislocation patterns in near-surface and core regions of deformed nickel polycrystals with few grains across the cross section. *Mech. Mater.* **2010**, *42*, 44–54. [CrossRef]

60. Balogh, L.; Gubicza, J.; Hellmig, R.J.; Estrin, Y.; Ungár, T. Thermal stability of the microstructure of severely deformed copper. *Zeitschrift fur Kristallographie* **2006**, *2*, 381–386. [CrossRef]

61. Gubicza, J.; Nam, N.H.; Balogh, L.; Hellmig, R.J.; Stolyarov, V.V.; Estrin, Y.; Ungár, T. Microstructure of severely deformed metals determined by X-ray peak profile analysis. *J. Alloys Compd.* **2004**, *378*, 248–252. [CrossRef]

62. Christian, J.W.; Mahajan, S. Deformation twinning. *Prog. Mater. Sci.* **1995**, *39*, 1–157. [CrossRef]

63. Karaman, I.; Yapici, G.G.; Chumlyakov, Y.I.; Kireeva, I.V. Deformation twinning in difficult-to-work alloys during severe plastic deformation. *Mater. Sci. Eng. A* **2005**, *410–411*, 243–247. [CrossRef]

64. Yapici, G.G.; Karaman, I.; Luo, Z.P. Mechanical twinning and texture evolution in severely deformed Ti-6Al-4V at high temperatures. *Acta Mater.* **2006**, *54*, 3755–3771. [CrossRef]

65. Glavicic, M.G.; Salem, A.A.; Semiatin, S.L. X-ray line-broadening analysis of deformation mechanisms during rolling of commercial-purity titanium. *Acta Mater.* **2004**, *52*, 647–655. [CrossRef]

66. Byun, T.S.; Lee, E.H.; Hunn, J.D. Plastic deformation in 316LN stainless steel—Characterization of deformation microstructures. *J. Nucl. Mater.* **2003**, *321*, 29–39. [CrossRef]

67. Lee, W.-S.; Lin, C.-F. Impact properties and microstructure evolution of 304L stainless steel. *Mater. Sci. Eng. A* **2001**, *308*, 124–135. [CrossRef]

68. Zhang, P.; Chen, Y.; Xiao, W.; Ping, D.; Zhao, X. Twin structure of the lath martensite in low carbon steel. *Prog. Nat. Sci. Mater. Int.* **2016**, *26*, 169–172. [CrossRef]

69. Tian, Y.; Gorbatov, O.I.; Borgenstam, A.; Ruban, A.V.; Hedström, P. Deformation Microstructure and Deformation-Induced Martensite in Austenitic Fe-Cr-Ni Alloys Depending on Stacking Fault Energy. *Metall. Mater. Trans. A Phys. Metall. Mater. Sci.* **2017**, *48*, 1–7. [CrossRef]

70. Hansen, N.; Huang, X.; Pantleon, W.; Winther, G. Grain orientation and dislocation patterns. *Philos. Mag.* **2006**, *86*, 3981–3994. [CrossRef]

71. Dillamore, I.L.; Katoh, H. The Mechanisms of Recrystallization in Cubic Metals with Particular Reference to Their Orientation-Dependence. *Met. Sci.* **1974**, *8*, 73–83. [CrossRef]

72. Hughes, D.A.; Hansen, N. Microstructure and Stength of Nickel at Large Strains. *Acta Mater.* **2000**, *48*, 2985–3004. [CrossRef]

73. Kocks, U.F.; Mecking, H. Physics and phenomenology of strain hardening: The FCC case. *Prog. Mater. Sci.* **2003**, *48*, 171–273. [CrossRef]

74. Čížek, J.; Janeček, M.; Krajňák, T.; Stráská, J.; Hruška, P.; Gubicza, J.; Kim, H.S. Structural characterization of ultrafine-grained interstitial-free steel prepared by severe plastic deformation. *Acta Mater.* **2016**, *105*, 258–272. [CrossRef]

75. Gubicza, J.; Chinh, N.Q.; Krallics, G.; Schiller, I.; Ungár, T. Microstructure of ultrafine-grained fcc metals produced by severe plastic deformation. *Curr. Appl. Phys.* **2006**, *6*, 194–199. [CrossRef]

76. Humphreys, F.J.; Hatherly, M. *Recrystallization and Related Annealing Phenomena*; Elsevier: New York, NY, USA, 2004. [CrossRef]

77. Driver, J.H.; Theyssier, M.-C.; Maurice, C.I. Electron backscattered diffraction microtexturestudies on hot deformed aluminium crystals. *Mater. Sci. Technol.* **1996**, *12*, 851–858. [CrossRef]

78. Popova, E.; Staraselski, Y.; Brahme, A.; Mishra, R.K.; Inal, K. Coupled crystal plasticity—Probabilistic cellular automata approach to model dynamic recrystallization in magnesium alloys. *Int. J. Plast.* **2015**, *66*, 85–102. [CrossRef]

79. Murty, K.L.; Charit, I. Texture development and anisotropic deformation of zircaloys. *Prog. Nucl. Energy* **2006**, *48*, 325–359. [CrossRef]

80. Arafin, M.A.; Szpunar, J.A. A new understanding of intergranular stress corrosion cracking resistance of pipeline steel through grain boundary character and crystallographic texture studies. *Corros. Sci.* **2009**, *51*, 119–128. [CrossRef]

81. Das, Y.B.; Simm, T.H.; Gungor, S.; Fitzpatrick, M.E.; Forsey, A.N.; Moat, R.J. An experimental study of plastic deformation and transformation in austenitic stainless steel. Unpubl. Work. (n.d.). 1–35.

82. Bachmann, F.; Hielscher, R.; Schaeben, H. Grain detection from 2d and 3d EBSD data—Specification of the MTEX algorithm. *Ultramicroscopy* **2011**, *111*, 1720–1733. [CrossRef] [PubMed]

83. Lütjering, G.; Williams, J. *Titanium*, 2nd ed.; Springer: Berlin, Germany, 2007.

84. Honeycombe, R.W.K. *The Plastic Deformation of Metals*; Edward Arnold: Maidenhead, UK, 1984.

85. Máthis, K.; Csiszár, G.; Čapek, J.; Gubicza, J.; Clausen, B.; Lukáš, P.; Vinogradov, A.; Agnew, S.R. Effect of the loading mode on the evolution of the deformation mechanisms in randomly textured magnesium polycrystals—Comparison of experimental and modeling results. *Int. J. Plast.* **2015**, *72*, 127–150. [CrossRef]

86. Máthis, K.; Nyilas, K.; Axt, A.; Dragomir-Cernatescu, I.; Ungár, T.; Lukáč, P. The evolution of non-basal dislocations as a function of deformation temperature in pure magnesium determined by X-ray diffraction. *Acta Mater.* **2004**, *52*, 2889–2894. [CrossRef]

87. Dragomir, I.C.; Li, D.S.; Castello-Branco, G.A.; Garmestani, H.; Snyder, R.L.; Ribarik, G.; Ungár, T. Evolution of dislocation density and character in hot rolled titanium determined by X-ray diffraction. *Mater. Charact.* **2005**, *55*, 66–74. [CrossRef]

88. Dragomir, I.C.; Castello-Branco, G.A.; Ribarik, G.; Garmestani, H.; Ungár, T.; Snyder, R.L. Burgers vector populations in hot rolled titanium determined by X-ray peak profile analysis. *Zeitschrift fur Kristallographie* **2006**, *1*, 99–104. [CrossRef]

89. Schafler, E.; Nyilas, K.; Bernstorff, S.; Zeipper, L.; Zehetbauer, M.; Ungár, T. Microstructure of post-deformed ECAP- Ti investigated by Multiple X-Ray Line Profile Analysis. *Zeitschrift fur Kristallographie* **2006**, *23*, 129–134. [CrossRef]

90. Ungár, T.; Castelnau, O.; Ribarik, G.; Drakopoulos, M.; Bachade, J.L.; Chauveau, T.; Snigirev, A.; Snigireva, I.; Schroer, C.; Bacroix, B. Grain to grain slip activity in plastically deformed Zr determined by X-ray micro-diffraction line profile analysis. *Acta Mater.* **2007**, *55*, 1117–1127. [CrossRef]

91. Long, F.; Balogh, L.; Daymond, M.R. Evolution of dislocation density in a hot rolled Zr–2.5Nb alloy with plastic deformation studied by neutron diffraction and transmission electron microscopy. *Philos. Mag.* **2017**, *97*, 2888–2914. [CrossRef]

92. Ungár, T.; Holden, T.M.; Jóni, B.; Clausen, B.; Balogh, L.; Csiszár, G.; Brown, D.W. Dislocation structure in different texture components determined by neutron diffraction line profile analysis in a highly textured Zircaloy-2 rolled plate. *J. Appl. Crystallogr.* **2015**, *48*. [CrossRef]

93. Wilkens, M. *Fundamental Aspects of Dislocation Theory*; Natl. Bur. Stand. (US)Spec. Publ. No. 317; U.S. Department of Commerce National Bureau of Standards: Washington, DC, USA, 1970.

94. Simm, T.H.; Das, Y.; Dunlop, T.; Perkins, K.M.; Birosca, S.; Prakash, L.; da Fonseca, J.Q. In situ and ex situ measurements and modelling of the plastic deformation of HCP alloys measured by neutron diffraction. Unpubl. Work. N/A (2018).

95. Timár, G.; da Fonseca, J.Q. Modeling Twin Clustering and Strain Localization in Hexagonal Close-Packed Metals. *Metall. Mater. Trans. A Phys. Metall. Mater. Sci.* **2014**, *45*, 5883–5890. [CrossRef]

96. Lutjering, G.; Williams, J.C. Commercially Pure (CP) Titanium and Alpha Alloys. *Titanium* **2007**, 175–201. [CrossRef]

97. Staroselsky, A.; Anand, L. A constitutive model for hcp materials deforming by slip and twinning: Application to magnesium alloy AZ31B. *Int. J. Plast.* **2003**, *19*, 1843–1864. [CrossRef]

98. Zaefferer, S. A study of active deformation systems in titanium alloys: Dependence on. *Mater. Sci. Eng. A* **2003**, *344*, 20–30. [CrossRef]

99. Evans, C. Micromechanisms and Micromechanics of Zircaloy-4. Ph.D. Thesis, Imperial College London, London, UK, 2014.

100. Britton, T.B.; Dunne, F.P.E.; Wilkinson, A.J. On the mechanistic basis of deformation at the microscale in hexagonal close-packed metals. *Proc. R. Soc. A Math. Phys. Eng. Sci.* **2015**, *471*, 20140881. [CrossRef]

101. Zaefferer, S. Investigation of the Correlation between Texture and Microstrucure on a Submicrometer Scale in the TEM. *Adv. Eng. Mater.* **2003**, *5*, 745–752. [CrossRef]

102. Bridier, F.; Villechaise, P.; Mendez, J. Analysis of the different slip systems activated by tension in a α/β titanium alloy in relation with local crystallographic orientation. *Acta Mater.* **2005**, *53*, 555–567. [CrossRef]

103. Battaini, M.; Pereloma, E.V.; Davies, C.H.J. Orientation effect on mechanical properties of commercially pure titanium at room temperature. *Metall. Mater. Trans. A Phys. Metall. Mater. Sci.* **2007**, *38*, 276–285. [CrossRef]

104. Liu, Q.; Hansen, N. Deformation microstructure and orientation of F.C.C. crystals. *Phys. Status Solidi Appl. Res.* **1995**, *149*, 187–199. [CrossRef]

105. Bozzolo, N.; Chan, L.; Rollett, A.D. Misorientations induced by deformation twinning in titanium. *J. Appl. Crystallogr.* **2010**, *43*, 596–602. [CrossRef]

106. Mullins, S.; Patchett, B.M. Deformation microstructures in titanium sheet metal. *Metall. Trans. A* **1981**, *12*, 853–863. [CrossRef]

107. Liu, Y.; Yang, D.Z.; He, S.Y.; Wu, W.L. Microstructure developed in the surface layer of Ti-6Al-4V alloy after sliding wear in vacuum. *Mater. Charact.* **2003**, *50*, 275–279. [CrossRef]

108. Wertheim, G.K.; Butler, M.A.; West, K.W.; Buchanan, D.N.E. Determination of the Gaussian and Lorentzian content of experimental line shapes. *Rev. Sci. Instrum.* **1974**, *45*, 1369. [CrossRef]

109. Guan, D.; Rainforth, W.M.; Ma, L.; Wynne, B.; Gao, J. Twin recrystallization mechanisms and exceptional contribution to texture evolution during annealing in a magnesium alloy. *Acta Mater.* **2017**, *126*, 132–144. [CrossRef]

110. Gong, N.; Wu, H.-B.; Yu, Z.-C.; Niu, G.; Zhang, D. Studying Mechanical Properties and Micro Deformation of Ultrafine-Grained Structures in Austenitic Stainless Steel. *Metals* **2017**, *7*, 188. [CrossRef]

111. Lee, E.H.; Byun, T.S.; Hunn, J.D.; Yoo, M.H.; Farrell, K.; Mansur, L.K. On the origin of deformation microstructures in austenitic stainless steel: Part I—Microstructures. *Acta Mater.* **2001**, *49*, 3269–3276. [CrossRef]

112. Balogh, L.; Niezgoda, S.R.; Kanjarla, A.K.; Brown, D.W.; Clausen, B.; Liu, W.; Tomé, C.N. Spatially resolved in situ strain measurements from an interior twinned grain in bulk polycrystalline AZ31 alloy. *Acta Mater.* **2013**, *61*, 3612–3620. [CrossRef]